Genetic ablation of neuronal mitochondrial calcium uptake halts Alzheimer's disease progression

Pooja Jadiya[1], Devin W. Kolmetzky[1], Dhanendra Tomar[1], Manfred Thomas[1], Henry M. Cohen[1], Salman Khaledi[1], Joanne F. Garbincius[1], Alycia N. Hildebrand and John W. Elrod[1]*

[1] Aging + Cardiovascular Discovery Center, Department of Cardiovascular Sciences, Lewis Katz School of Medicine at Temple University, Philadelphia, PA 19140

Conflict of interest: The authors have no financial conflict of interest to report.

***Correspondence:**

John W. Elrod, PhD

Director, Aging + Cardiovascular Discovery Center

Lewis Katz School of Medicine at Temple University

3500 N Broad St, MERB 949

Philadelphia, PA 19140

elrod@temple.edu

elrodlab.org

Abstract

Alzheimer's disease (AD) is characterized by the extracellular deposition of amyloid beta, intracellular neurofibrillary tangles, synaptic dysfunction, and neuronal cell death. These phenotypes correlate with and are linked to elevated neuronal intracellular calcium ($_{i}Ca^{2+}$) levels. Recently, our group reported that mitochondrial calcium ($_{m}Ca^{2+}$) overload, due to loss of $_{m}Ca^{2+}$ efflux capacity, contributes to AD development and progression. We also noted proteomic remodeling of the mitochondrial calcium uniporter channel (mtCU) in sporadic AD brain samples, suggestive of altered $_{m}Ca^{2+}$ uptake in AD. Since the mtCU is the primary mechanism for Ca^{2+} uptake into the mitochondrial matrix, inhibition of the mtCU has the potential to reduce or prevent $_{m}Ca^{2+}$ overload in AD. Here, we report that neuronal-specific loss of mtCU-dependent $_{m}Ca^{2+}$ uptake in the 3xTg-AD mouse model of AD reduced Aβ and tau-pathology, synaptic dysfunction, and cognitive decline. Knockdown of *Mcu* in a cellular model of AD significantly decreased matrix Ca^{2+} content, oxidative stress, and cell death. These results suggest that inhibition of neuronal $_{m}Ca^{2+}$ uptake is a novel therapeutic target to impede AD progression.

Introduction

Alzheimer's disease (AD) is associated with mitochondrial dysfunction (1-3) and impaired neuronal intracellular calcium ($_iCa^{2+}$) homeostasis (4, 5). However, little is known about the precise mechanisms underlying AD. Many studies point to increased $_iCa^{2+}$ as an important upstream mechanism that may promote β-amyloid (Aβ) and tau pathology and so contribute to AD pathogenesis (6-8). Excessive $_iCa^{2+}$ can result from the dysregulation of membrane-embedded Ca^{2+}-permeable channels, such as voltage-operated channels like calcium homeostasis modulator 1 (CALHM1) (9), amino-3-hydroxy-5-methyl-4-isoxazolepropionic acid receptors (AMPAR) (10), or N-methyl-D-aspartate receptors (NMDAR) (5). Further, alterations in store-operated calcium entry (SOCE) (11) and increased ryanodine receptor (RyR) (12) and inositol trisphosphate receptor (IP3R) activity are reported to increase ER calcium content in the context of AD (13). This coupled with the reports of increased coupling of mitochondria with the ER (14, 15) provides a clear avenue towards mitochondrial calcium overload.

In contrast, other studies suggest that Aβ pathologies are upstream of impaired neuronal $_iCa^{2+}$ handling (16) and mitochondrial dysfunction (17), leading to cognitive impairment, synaptic dysfunction, and neurodegeneration in AD. For example, mutations in PS1 are reported to cause RyR hyperactivity (18) and increased IP3R channel gating (19, 20) that lead to exaggerated $_iCa^{2+}$ signaling. FAD mutant PS1 (M146L) interacts with the IP3R, which results in increased Ca^{2+} release from the ER and functional consequences of this interaction (IP3R-PS1) stimulate APP processing (20), leading to AD- pathologies. The further study suggests that this increased $_iCa^{2+}$ signaling through IP_3R-PS1 interaction is a disease-specific mechanism in FAD (19), enhancing the production of reactive oxygen species that may contribute to AD pathogenesis (21). Similarly, post-translational remodeling (PKA

phosphorylation, oxidation, and nitrosylation) of neuronal RyR2 channels in human AD patients and murine models of AD induces ER-calcium leak that activates Ca^{2+}-dependent signaling pathways, including calpain activation, tau phosphorylation, and cognitive deficits (18). Thus, mitochondrial ionic dysregulation and dysfunctions which could be possibly initiated by altered ER-ionic homeostasis precede Aβ and tau pathology.

Elevations in $_{i}Ca^{2+}$ are theorized to be rapidly integrated into mitochondria due to the high electromotive force across the inner mitochondrial membrane (IMM) generated by the electron transport chain ($\Delta\psi$ = ~ -160mv). The ever-changing $_{i}Ca^{2+}$ environment and high driving force for mitochondrial calcium ($_{m}Ca^{2+}$) entry require that neuronal mitochondria possess a tightly controlled $_{m}Ca^{2+}$ exchange system (22, 23). Ca^{2+} enters the mitochondria matrix via the mitochondrial calcium uniporter channel complex (mtCU) and modulates key metabolic control points in the TCA cycle (24, 25). Thus, it is postulated that $_{m}Ca^{2+}$ uptake is the signal that matches mitochondrial energy production to neuronal energy demand.

However, excessive $_{m}Ca^{2+}$ uptake is linked with mitochondrial dysfunction and causes opening of mitochondrial permeability transition pore (mPTP) which leads to oxidative stress and cell death (1, 26-28), both of which are contributors to AD. We recently reported that $_{m}Ca^{2+}$ overload due to loss of NCLX, the mitochondrial sodium-calcium exchanger, and the main mechanism for $_{m}Ca^{2+}$ efflux, contributes to AD progression in the 3xTg-AD mouse model (29). We also noted proteomic remodeling of the mtCU in sporadic AD patients (29). In support of our findings, a recent study showed increased neuronal $_{m}Ca^{2+}$ levels correlated with plaque deposition in the APP/PS1-Tg mouse model (30), and numerous studies have implicated $_{m}Ca^{2+}$ overload in the activation of cell death and neurodegeneration (28, 29, 31-34). For example, deletion of cyclophilin D (CypD), a necessary activator of the mPTP, has been shown to prevent mitochondrial dysfunction and memory impairments in AD models (1). Additionally, AD fibroblasts treated with cyclosporine A (CsA, a pharmacological inhibitor of

the mPTP) showed reduced mitochondrial ROS and improvements in mitochondrial function (35). Further, a recent study utilizing a *C. elegans* AD model, *sel-12* (homolog of presenilin) mutant, observed increased ER-mitochondria Ca^{2+} signaling that increased $_{m}Ca^{2+}$ uptake, resulting in increased ROS (reactive oxygen species) generation and neuronal dysfunction (36). Similarly, an AD-linked presenilin mutation (PS1) was reported to increase inositol triphosphate (IP3)-mediated Ca^{2+} transients (37) and ER-mitochondrial contacts in AD (15), both of which would contribute to $_{m}Ca^{2+}$ overload. These studies strengthen the notion that $_{m}Ca^{2+}$ overload is central to AD progression.

While many classical biophysical studies have characterized the properties of $_{m}Ca^{2+}$ flux in this disease, there have been virtually no causal studies defining the precise role of $_{m}Ca^{2+}$ uptake in AD pathogenesis. *Mitochondrial calcium uniporter* (*MCU*) encodes the channel-forming portion of the mtCU complex and is required for IMM Ca^{2+} permeation (38, 39). Previously, fibroblasts from AD patients displayed a significant increase in MCU protein expression compared to controls (35). Most notably, overexpression of MCU by stereotaxic injection of adenovirus into the cortex of mice resulted in increased mitochondrial Ca^{2+} levels, neuronal cell death, and gliosis (34), suggesting that $_{m}Ca^{2+}$ overload alone is sufficient to promote brain pathology. Since MCU is necessary for $_{m}Ca^{2+}$ uptake, genetic ablation has the potential to reduce or prevent $_{m}Ca^{2+}$ overload and downstream sequala. To study whether changes in $_{m}Ca^{2+}$ uptake contribute to the development of AD, we generated 3xTg-AD mutant mice with neuronal-specific deletion of *Mcu*. We report that loss of $_{m}Ca^{2+}$ uptake improves cognitive decline and ameliorates AD progression by reducing Aβ aggregation, tau phosphorylation and oxidative stress. The identification of a central role for $_{m}Ca^{2+}$ uptake in AD pathogenesis is a critical step towards developing novel therapeutic interventions with translational potential to combat this untreatable disease.

Results

Loss of neuronal $_mCa^{2+}$ uptake improves AD-associated cognitive deficits. To assess the role of $_mCa^{2+}$ uptake in AD pathology, we generated a neuronal-specific knockout of *Mcu* in the 3xTg-AD mutant mouse model. Mice expressing neuronal-restricted Cre recombinase (Camk2a-Cre) (40) were crossed with *Mcu* floxed mice (*Mcu*$^{fl/fl}$) (28) to generate restricted loss of MCU in frontal cortex and hippocampus (*Mcu*$^{fl/fl}$ x Camk2a-Cre). To investigate the impact of $_mCa^{2+}$ uptake in AD, we utilized the 3xTg-AD mouse model of familial AD-associated neuropathology and memory defects (41). These mice develop robust disease including both Aβ and tau pathology due to mutations in three genes including Presenilin 1 (*Psen1*, M146V knock-in), amyloid beta precursor protein (APP*swe*, KM670/671NL transgene) and microtubule associated protein tau (MAPT, P301L transgene). The neuronal-specific *Mcu* knockouts were crossed with 3xTg-AD mice (3xTg-AD x *Mcu*$^{fl/fl}$ x Camk2a-Cre, **Figure 1A**). Western blot analysis revealed loss of MCU protein in the frontal cortex of 2-month-old 3xTg-AD x *Mcu*$^{fl/fl}$ x Camk2a-Cre mice (**Figure 1B, S1A**) and a corresponding reduction in 12-month-old mice (**Figure 1C, S1H**). No significant changes in the expression of other mitochondrial calcium uniporter channel complex (mtCU)-associated components were observed (**Figure 1B-C, S1 A-N**). We next examined $_mCa^{2+}$ uptake and calcium retention capacity (CRC) using mitochondria isolated from the frontal cortex of 12-month-old mice with MCU deletion in the 3xTg-AD background. 3xTg-AD mice (red arrow in representative tracings) demonstrated a significant decrease in CRC with no significant increase in $_mCa^{2+}$ uptake rate compared with CamK2a-Cre controls (black arrow) (**Figure 1D-F**). The loss of neuronal MCU in 3xTg-AD mice (blue line) showed no CRC and near complete loss of $_mCa^{2+}$ uptake (calculated after first 5-μm Ca^{2+} bolus) compared to controls (**Figure 1D-F**).

AD is a debilitating neurodegenerative disorder, characterized by the loss of memory due to neuronal cell death in the hippocampus. To assess the effect of loss of neuronal $_mCa^{2+}$ uptake

on cognition, mice from all groups: Camk2a-Cre (non-AD control), 3xTg-AD x Camk2a-Cre (Cre-control for experimental group), and 3xTg-AD x *Mcu*$^{fl/fl}$ x Camk2a-Cre (experimental group) were tested for memory deficits using a Y-maze and fear-conditioning behavioral tests at 6, 9, 12 and 15 months of age. We evaluated spatial memory in the Y-maze test and found that loss of neuronal MCU significantly improved age-associated impairments in spatial working memory and exploratory memory, as indicated by increased alternations by mice from 9 - 15 months of age (**Figure 1G**). Importantly, we did not see any significant differences in locomotor ability between the groups, as indicated by an equivalent number of arm entries (**Figure 1H**).

Next, mice were tested in a fear-conditioning experiment to identify changes in contextual fear conditioning, a measure of hippocampus-dependent associative learning, and cued fear conditioning, a measure of amygdala-dependent associative learning. 3xTg-AD mice displayed impairments in contextual recall at 6 - 15 months of age (**Figure 1J**) and cued recall at 12 - 15 months of age (**Figure 1K**). AD mice with neuronal deletion of *Mcu* exhibited a significant improvement in contextual recall from 6 - 15 months of age (**Figure 1J**) and significant improvements in cued recall memory (**Figure 1K**). No differences in freezing response were observed during the training session between groups throughout the study, suggesting loss of MCU had no measurable effect on locomotor activity or baseline behavior (**Figure 1I**). Important for translational considerations, loss of neuronal MCU in wild-type mice (*Mcu*$^{fl/fl}$ x Camk2a-Cre) did not result in cognitive impairment in Y-maze testing (**Figure S1 O-P**). However, we did note a slight decrease in fear-conditioning contextual recall in 12 month-old mice (**Figure S1 Q-S**), perhaps suggesting a physiological role for $_{m}Ca^{2+}$ uptake in specific neuronal populations involved in long-term amygdala and/or hippocampus memory (42).

Genetic ablation of neuronal $_{m}Ca^{2+}$ uptake attenuates Aβ accumulation in 3xTg-AD mice. Neuronal $_{i}Ca^{2+}$ signaling dysfunction has been linked to Aβ aggregation and its associated pathology in AD (43-45). Therefore, we examined whether the protection against cognitive

decline afforded by ablating $_{m}Ca^{2+}$ uptake correlates with a reduction in amyloidogenic pathology. Brain cortex and hippocampus homogenates isolated from aged mice (15 months) were assayed by ELISA for $A\beta_{1-40}$ and $A\beta_{1-42}$ peptide levels in both RIPA-soluble and -insoluble (formic acid-soluble) fractions. 3xTg-AD mice have been reported to show Aβ plaque deposition as early as 6 months in the cortex and hippocampus (41). Increased levels of soluble and insoluble $A\beta_{1-40}$ and $A\beta_{1-42}$ peptides were found in both the cortex and hippocampus of 3xTg-AD mice. The loss of neuronal $_{m}Ca^{2+}$ uptake in AD mice resulted in a significant decrease in Aβ peptide levels in cortex and hippocampus, as well as a reduction in the $A\beta_{42/40}$ ratio in soluble fractions of brain cortex (**Figure 2A-D**; **S2A**). In addition, aged 3xTg-AD x *Mcu*$^{fl/fl}$ x Camk2a-Cre mice displayed a significant reduction (~40%) in amyloid deposits, as compared to 3xTg-AD x Camk2a-Cre experimental control mice (**Figure 2E, F**). To further investigate the mechanism by which genetic loss of *Mcu* reduces Aβ burden, we examined the expression of all known secretases involved in APP processing including α, β and γ-secretase (**Figure 2G; S2C)**. Compared to controls, significant increases in the expression of total APP, β (BACE-1) and γ-secretase complex components (PS1, NCT and APH1 subunit) were observed in aged 3xTg-AD, whereas α-secretase (ADAM10) expression was reduced (**Figure 2H; S2C- I**). Interestingly, loss of MCU in 3xTg-AD mice reverted the increased expression of γ-secretase complex associated proteins presenilin-1 (PS-1) and nicastrin (NCT) back towards wild-type levels (**Figure 2G; Figure S2C- I**). As expected for this transgenic model, no significant changes in the expression of total APP were observed (**Figure 2G; Figure S2C- D**). Semi-quantitative analysis of Western blots showed a trending decrease in cortex expression of β -secretase (BACE-1) (**Figure S2F)** and anterior pharynx-defective phenotype 1 (APH-1) component of the γ-secretase complex (**Figure S2I)** in 3xTg-AD x *Mcu*$^{fl/fl}$ x Camk2a-Cre brains. These findings suggest that loss of neuronal MCU decreases Aβ levels and deposition in AD, possibly by direct or indirect modulation of the γ-secretase pathway.

Loss of neuronal MCU expression decreases AD-associated tau pathology. Neurofibrillary tangles are considered a hallmark of AD histopathology and predominantly are comprised of hyper-phosphorylated tau. 15-month-old 3xTg-AD mice showed a significant increase in the expression of total tau (soluble and insoluble), and increased phosphorylation at all residues examined, as compared to non-AD controls (**Figure 3A-E; Figure S3A-C**), while 3xTg-AD x *Mcu*$^{fl/fl}$ x Camk2a-Cre mice displayed a significant reduction in insoluble tau (**Figure 3A-B; Figure S3A**) with no change in the levels of soluble tau (**Figure 3A; Figure S3A-B**). We also observed a striking reduction in S202/T205 (AT8 immunoreactivity), T231/ S235 (AT180 immunoreactivity) and Ser396 (PHF-13 immunoreactivity) phospho-tau (**Figure 3A-E)** and a variable reduction in T181 (AT270 immunoreactivity) with loss of neuronal $_{m}Ca^{2+}$ uptake (**Figure 3A; S3A, C)**. To validate our biochemical findings, we performed immunohistochemistry to examine tau phosphorylation specifically in pyramidal neurons of the CA1 region of the brain. There was a significant reduction in S202/T205 (~40%) and T231/ S235 (~34%) tau phosphorylation in *Mcu*-deleted 3xTg-AD, with no observed change in total soluble tau (**Figure 3F-H; Figure S3D**). These results suggest loss of neuronal $_{m}Ca^{2+}$ uptake is sufficient to retard tau pathology in AD.

Loss of neuronal mitochondrial calcium uptake reduces oxidative stress, improves synaptic integrity, and reduces neuroinflammation. Increased oxidative stress, neuroinflammation, and synaptic dysfunction are early cellular occurrences in AD pathogenesis (46, 47). To examine the effect of neuronal loss of $_{m}Ca^{2+}$ uptake on redox status, we utilized dihydroethidium (DHE) staining to monitor real-time superoxide generation in fresh brain slices and found a signficant reduction in ROS generation in the cortex and hippocampus of 3xTg-AD x *Mcu*$^{fl/fl}$ x Camk2a-Cre (**Figure 4A-C**) as compared to 3xTg-AD brains. Next, we assessed lipid peroxidation (oxidative degradation of lipids) by staining for 4-hydroxy-2-nonenal (4-HNE) in

aged AD mice and controls. 3xTg-AD x *Mcu*$^{fl/fl}$ x Camk2a-Cre displayed a ~30% decrease in 4-HNE staining in the cortex (**Figure 4D, E**) and hippocampus (**Figure 4D, F**).

Studies have revealed decreased synaptic plasticity and altered dendritic spines in excitatory glutamatergic synapses as an early indicator of pathology in AD (48-50). The vesicular protein, synaptophysin (SYP), is a marker of pre-synaptic integrity (51) and post-synaptic density protein (PSD-95) is a scaffolding protein localized at excitatory synapses (52) which plays an important role in the process of learning (53) and also in the coupling of NMDA receptors and K^+ channels at the post-synaptic membrane (54). We observed a significant reduction in both SYP and PSD-95 expression in the brains of AD mice which was corrected to non-disease, wild-type levels in the brains of 3xTg-AD x *Mcu*$^{fl/fl}$ x Camk2a-Cre mice (**Figure 4G; Figure S4A-B**).

Astrocytes and microglia activation are early features of AD-associated inflammation (55, 56). The expression of glial fibrillary acidic protein (GFAP), a marker of astrocyte reactivity (57), was significantly decreased in brain homogenates isolated from 3xTg-AD x *Mcu*$^{fl/fl}$ x Camk2a-Cre, when compared to 3xTg-AD mice, without any changes in ionized calcium binding adaptor molecule 1 (Iba1) expression, a marker of microglia activation (**Figure 4H; Figure S4C-D**).

To conclusively evaluate if changes in mitochondrial content occurred in our model system, we performed transmission electron microscopy (TEM) to examine in situ mitochondrial morphology. Four mice per genotype were examined and ~200 mitochondria were analyzed per sample by a blinded investigator for each brain tissue. No significant differences were observed in mitochondrial number per area and the distribution of mitochondrial shape (area, perimeter, circularity, Feret's diameter, aspect ratio) within all groups in the frontal cortex of 12-month-old mice (**Figure S4E-K**).

Similarly, quantification of the ratio of mtDNA vs. nDNA showed no change in mitochondrial content in 3xTg-AD × Camk2a-Cre and 3xTg-AD × *Mcu*$^{fl/fl}$ × Camk2a-Cre and Camk2a-Cre at 2-

& 12-month age. We didn't find any change in mitochondria mass between the groups at two timepoints (**Figure S4L**), but our data does support that mitochondrial mass may decrease with age. All together, these results suggest that decreasing $_{m}Ca^{2+}$ uptake during AD pathogenesis reduces oxidative stress and inflammation and preserves synaptic integrity without any change in morphology and mass.

Loss of $_{m}Ca^{2+}$ uptake prevents AD-associated mitochondrial dysfunction. To directly examine mitochondrial consequences of *Mcu* loss and the molecular mechanisms affording neuroprotection, we utilized a neuroblastoma cell line harboring a transgene for the well characterized Swedish mutation (N2a-APPswe: K670N, M671L) (58). We transduced control (N2a) and APPswe cells with lentivirus encoding shRNA targeting *Mcu*. Western blot analysis revealed ~55% loss of MCU protein in shRNA stable knockdown cells, as compared to scramble shRNA control cells (Scr-shRNA) (**Figure 5B, C**). We did not see any significant changes in the expression of other $_{m}Ca^{2+}$ exchange associated proteins after knockdown of *Mcu*. However, similar to what we previously reported in sporadic AD patients (29), in APPswe cells we did see significant decreases in the expression of the mtCU regulators MICU1, MICU2, and MCUB (59-62) and the loss of these proteins suggest a predisposition towards increased $_{m}Ca^{2+}$ uptake and overload (**Figure 5B; Figure S5 A-D**). Attenuation of $_{m}Ca^{2+}$ uptake in *Mcu* knockdown cells was validated in a permeabilized cell system using the ratiometric reporters FuraFF (Ca^{2+}) and JC1 ($\Delta\psi$) (**Figure 5D, E; Figure S5E**). To evaluate matrix free-Ca^{2+} content, cells from all groups were permeabilized with digitonin and treated with thapsigargin to inhibit SERCA, and then treated with FCCP to release all matrix free-Ca^{2+}, as previously reported (28, 29). APPswe cells were found to have an increased level of matrix Ca^{2+} as compared to N2a controls. Knockdown of *Mcu* in APPswe cell lines significantly decreased the matrix free-Ca^{2+} content, back towards control levels (**Figure 5F, G**). These data suggest that amyloid accumulation perturbs $_{m}Ca^{2+}$ uptake and promotes matrix Ca^{2+} overload. In addition, we

measured changes in mitochondrial membrane potential in N2a and APPswe cells +/- Mcu, independent of cytosolic calcium flux (permeabilization) and independent of SR content or flux (thapsigargin) and show that loss of MCU did not directly impact mitochondrial membrane potential (**Figure S5H, I**). A number of studies suggest a strong association between $_{m}Ca^{2+}$ overload, oxidative stress and metabolic dysfunction (28, 36, 63, 64) and both are causal contributors to AD progression. To examine redox status in 3xTg-AD mice we measured total cellular ROS content using the CellRox assay and mitochondrial superoxide production using the MitoSOX Red reporter. AD-mutant cell lines displayed enhanced ROS levels (total and mitochondrial), and both were reduced with loss of MCU (**Figure 5H, I**). To further evaluate MCU-mediated mechanisms of cytoprotection, cells from all groups were examined for plasma membrane rupture and viability following treatment with ionomycin (Ca^{2+} stress), and *tert*-butyl hydroperoxide (ROS stressor). We observed a significant decrease in membrane rupture, a characteristic of necrotic cell death, and enhanced cellular viability in *Mcu* knockdown APPswe cell lines (**Figure 5J, K; Figure S5 F-G**). All together, these results suggest that the inhibition of $_{m}Ca^{2+}$ uptake in AD rescues metabolic dysfunction, redox imbalance, and cell death.

Discussion

We report that neuronal loss of MCU in familial 3xTg-AD mice prevents AD-pathology and age-dependent cognitive decline. However, its role in sporadic AD needs to be determined. We believe that efficacious treatment of familial AD may initiate relevant therapeutics for sporadic AD. While previous studies provide ample anecdotal and supportive evidence of mitochondrial dysfunction resulting from $_{m}Ca^{2+}$ overload (4, 12, 13), the data we present here suggests a causal role for dysregulated $_{m}Ca^{2+}$ uptake as an early pathogenic mechanism in AD development. For example, glutamate excitotoxicity due to excessive $_{i}Ca^{2+}$ promotes neuronal dysfunction in many neurological diseases (65-67), and MCU overexpression worsens excitotoxic cell death (33), implicating $_{m}Ca^{2+}$ uptake in this process. Also, previous experiments in a late-onset familial Parkinson's disease (PD) model indicate that $_{m}Ca^{2+}$ overload is sufficient to cause dendritic degeneration (8). Further, inactivation of MCU either pharmacologically by ruthenium red or genetically is neuroprotective in *pink1*$^{-/-}$ zebrafish models of PD (68, 69). Strong correlative evidence that mtCU dysregulation is sufficient to cause brain and skeletal muscle disorders is seen in patients with loss of function mutations in MICU1 (32). Indirect evidence from reports of increased ER-mitochondria crosstalk (15) and Ca^{2+} transfer in AD (70), also may contribute to increased $_{m}Ca^{2+}$ content. Indeed, neuronal cells expressing apolipoprotein E4 (apoE4), a major genetic risk factor for AD, displayed increased levels of $_{m}Ca^{2+}$ and ER-mitochondria tethering which promoted mitochondrial impairments and neuronal dysfunction (71).

Overwhelming evidence suggests that amyloid precursor protein, its processing proteins β- and γ-secretase (72), as well as Aβ localize within the mitochondria and in mitochondria-associated membranes (MAMs) (73). The interactions between mitochondrial proteins and amyloid are reported to cause mitochondrial dysfunction, oxidative stress, metabolic failure (17, 74), and impair mitochondrial proteostasis (75). Furthermore, it has been reported that Aβ modifies

mitochondria -ER contact sites and increases the ER release of Ca^{2+} (15, 76), potentially promoting $_{m}Ca^{2+}$ uptake. In addition, while somewhat controversial, it's thought that Aβ oligomers can form calcium-permeable pores in the mitochondrial membrane, promoting excessive Ca^{2+} entry, opening of the mPTP, and cell death (77, 78). Similarly, the accumulation of tau alters ER-mitochondria apposition and thereby may also contribute to AD (79). These results indicate that $_{m}Ca^{2+}$ overload may be a central mediator of AD progression, upstream and downstream of Aβ, and support the hypothesis that the reduction of $_{m}Ca^{2+}$ uptake in AD may be a powerful therapeutic approach.

Our results demonstrate that reducing $_{m}Ca^{2+}$ uptake in a robust AD animal model is sufficient to prevent neuropathology and cognitive decline. The exact mechanism for this beneficial effect is not fully elucidated, but we believe it is likely a combinatorial effect of decreasing mitochondrial ROS, preserving energetics, and inhibiting cell death signaling. The AD brain is extremely vulnerable to redox imbalance due to the high neuronal energy demand and supporting metabolism to maintain OxPhos. The increased expression and activity of β and γ secretase, and increased phosphorylation of tau are associated with oxidative stress (80), mitochondrial dysfunction (81, 82), and impaired energy metabolism (81). The link between Ca^{2+} and oxidative stress is supported by several previous reports. For example, elevated $_{i}Ca^{2+}$ enhances oxidative stress in neurons and astrocytes (83). Moreover, the loss of MICU1 and a resultant increase in $_{m}Ca^{2+}$ uptake elicits mitochondrial superoxide generation (59) and is linked with excitotoxicity (84). In contrast, the inhibition of $_{m}Ca^{2+}$ uptake reduces NMDAR-induced excitotoxicity and neuronal cell death (85). Previous experiments support that inhibition of mtCU $_{m}Ca^{2+}$ uptake either by RU360 treatment or siRNA targeting *Mcu,* decreases oxidative stress in cultured microglial cells (86) and in primary cerebellar granule neurons (CGNs) (87). Consistent with these findings, increased MCU activity is sufficient to promote oxidative stress (39, 87). Moreover, the increase of ER-mitochondrial calcium transfer in *PSEN* mutants is linked to high

ROS production (36). Thus, as reported here, increased $_{m}Ca^{2+}$ content in AD can drive excess ROS production, furthering neuronal dysfunction and disease progression.

Another important mechanism contributing to the neuroprotective consequences of MCU loss may be the reduction of gliosis. Recently, neuronal MCU overexpression (with adenovirus encoding MCU) into the cortex of mice showed increased immunohistochemical staining for GFAP (34). Our current results are in line with this observation, as we found a reduction in neuroinflammation with the ablation of $_{m}Ca^{2+}$ uptake. Furthermore, another mechanism of reduced gliosis in AD may be preservation of synaptic integrity, as a growing number of studies correlate enhanced gliosis with loss of PSD-95 (88). However, the specific direct or indirect mechanisms by which defective $_{m}Ca^{2+}$ exchange modulates the functional synaptic unit and gliosis in AD, remains to be determined.

Altogether, disruption of $_{m}Ca^{2+}$ exchange is an early upstream event that initiates AD pathology by interrupting many different cellular processes (e.g., metabolism, redox, protein aggregation, and inflammation). Our current findings support the inhibition of pathogenic $_{m}Ca^{2+}$ overload in AD as a novel therapeutic target. However, why $_{m}Ca^{2+}$ uptake increases in the AD pathogenesis is still unclear. Undoubtedly, neurons require a high energy supply for numerous functions such as synaptic transmission, action potential firing, and synapse development (89, 90) and are highly dependent on mitochondria to produce ATP (~93%) via OxPhos (91). Being highly mobile organelles, the subcellular localization of mitochondria greatly impacts individual cellular activities. Mitochondria in the synapse are a primary energy source for neuronal activity and neurotransmitter release and, ultimately, crucial in the learning and memory process (91, 92). In the synapse, where $_{i}Ca^{2+}$ cycles to high levels during depolarization, mitochondria buffer Ca^{2+} to shape the local $_{c}Ca^{2+}$ transients (22).

We hypothesize that neurons initially elevate $_mCa^{2+}$ uptake to increase ATP production by increasing the TCA cycle rate-limiting enzymes (PDH, α-KGDH, and ICDH) in the context of AD stress (93, 94). Mitochondrial matrix calcium can be increased by decreasing NCLX-dependent $_mCa^{2+}$ efflux or reducing the threshold for mtCU Ca^{2+} uptake by decreasing MICU1 protein levels or reducing MCUB inhibitory activity on the mtCU complex. These molecular phenomena were observed early in this AD model(29), suggesting that initially, it could be an adaptive response to augment cellular energetics during stress, which subsequently becomes maladaptive and results in $_mCa^{2+}$ overload, mtCU function impairment, and cell death induction. It is also known that aged or damaged mitochondria have a lower calcium buffering capacity and are more susceptible to calcium overload (95), which further supports mtCU dysregulation in AD**.** We previously demonstrated that $_mCa^{2+}$ homeostasis can be restored by increasing NCLX $_mCa^{2+}$ efflux, in AD (29) and here we provide strong evidence that reducing mtCU $_mCa^{2+}$ uptake lessens AD progression. Translational studies are needed to determine the most efficacious way to target $_mCa^{2+}$ dysregulation in AD, but here we have provided strong evidence that mitochondrial calcium is a causal contributor to AD pathogenesis.

Methods

Neuronal specific *Mcu* knockout 3xTg-AD mutant mouse. *Mcu* floxed mice were generated as reported previously by our lab (Luongo et al., 2015) by acquiring targeted ES cells made by recombinant insertion of a construct containing loxP sites flanking exons 5 - 6 of the *Mcu* gene (ch10: 58930544-58911529). Mutant ES cell lines were confirmed by PCR and injected into C57BL/6N blastocysts with subsequent transplantation into pseudo- pregnant females. Germline mutant mice were crossed with ROSA26-FLPe knock-in mice for removal of the FRT-flanked neomycin resistance cassette. Resultant homozygous *Mcu*$^{fl/fl}$ mice were crossed with neuron specific-Cre transgenic mice, *Camk2a*, to generate neuron-specific *Mcu* knockouts. The Calcium/calmodulin-dependent protein kinase II alpha (*Camk2a*) promoter drives Cre recombinase expression in the forebrain, specifically in the cortex and hippocampus (40). Resultant neuronal-specific loss-of-function models (*Mcu*$^{fl/fl}$ x Camk2a-Cre) were crossed with 3xTg-AD mutant mouse (41) to generate 3xTg-AD x *Mcu*$^{fl/fl}$ x Camk2a-Cre mutant mice. 3xTg-AD mice harbors three mutations: human Psen1 mutation (PS1^{M146V} knock-in), human amyloid precursor protein Swedish mutation (APP^{Swe} KM670/671NL), and P301L mutation of human tau (tau^{P301L}).

Cell cultures and stable cell lines. Mouse neuroblastoma N2a cells (Control) and N2a cells stably expressing human APP with the K670N/M671L Swedish mutation (APPswe) were propagated in Dulbecco's modified Eagle's medium containing 10% fetal bovine serum and 1% penicillin/streptomycin. Cells were maintained at 37°C in a humidified 5% CO2 incubator. APPswe cells were grown in the presence of 400 µg/mL G418 (29). Differentiation of N2a and APPswe was performed using standard protocols described earlier (29, 96) in media containing 50% Dulbecco's modified Eagle's medium (DMEM) and 50% OPTI-MEM with 1% penicillin/streptomycin for 72 hrs (29). Cells were seeded onto poly-D-lysine coated glass coverslips for all imaging studies.

To generate *Mcu* knockdown stable N2a/APP cells, we transduced cells with lentivirus encoding shRNA targeting *Mcu* for 16 hrs. in the presence of 4mg/ml polybrene. Stably transduced cells were selected with puromycin (2 mg/ml) 48 hrs. post transduction for one week and expanded. Knockdown of *Mcu* was evaluated by Western blot.

Immunohistochemistry. Mouse brains were dissected longitudinally at the center, and half of the brain was frozen on dry ice for biochemical analysis. The other was used for immunohistochemistry as previously described (29). In brief, brains were immersion-fixed in 4% paraformaldehyde (PFA) for 24 hrs. and embedded in paraffin. Serially sectioned (6-μm thick) brains were then deparaffinized, hydrated, and blocked in 2% fetal bovine serum. Sections were incubated overnight at 4 °C with following primary antibodies, monoclonal anti-β-amyloid, 17-24 (Aβ-4G8) dilution 1:150, HT7 dilution 1:150, phospho-tau (pThr231) monoclonal AT180 dilution 1:50, phospho-Tau (Ser202, Thr205) monoclonal AT8 dilution 1:50, anti-4 hydroxynonenal antibody (4-HNE) dilution 1:20, and then incubated with secondary antibody. The Vector Elite ABC system, an avidin/biotin-based peroxidase method, was used with diaminobenzidine, as the chromogen, to visualize immunoreactivity.

Biochemical and Western blot analysis. Protein samples from frontal cortex and hippocampus of mouse brains as well as from cell lysates were lysed using a 1x RIPA lysis buffer with SIGMAFAST™ Protease Inhibitor Cocktail and phosphatase inhibitor for the soluble fractions. After ultracentrifugation at 90,720×*g* for 45 min at 4°C, the supernatant was kept as the soluble fraction. The pellet was then sonicated in the presence of 70% formic acid and ultracentrifuged at 90,720×*g* for 45 min at 4°C. The resulting formic acid-extracted supernatant representing the insoluble fraction was neutralized with 6 N sodium hydroxide. $A\beta_{1-40}$ and $A\beta_{1-42}$ levels both in soluble and insoluble fractions were assayed using the method described in the manual of Human beta-Amyloid (1-40) ELISA Kit and Human beta-Amyloid (1-42) ELISA Kit, respectively. The monoclonal antibody BAN50, specifically detects the N-terminal of human

$A\beta_{1-16}$, was used to capture $A\beta_{1-40}$ and $A\beta_{1-42}$ in samples. Captured $A\beta_{1-40}$ and $A\beta_{1-42}$ was recognized by BA27 F(Aβ')2-HRP antibody, and BC05 F(Aβ')2-HRP, respectively. Both BA27 and BC05 are mAβ that specifically detect the C-terminal of Aβ. The TMB based color development was used to assess the HRP activity, and absorbance was then measured at 450 nm. Values were presented as a percentage of $A\beta_{1-40}$ and $A\beta_{1-42}$ secreted relative to control.

For Western blot analysis, the protein samples were quantified using Bio-Rad Protein Assay Dye Reagent. Equal amounts of proteins were resolved by electrophoresis on SDS-PAGE gels and transferred to a PVDF Immobilon-FL membrane (EMD Millipore, Catalog # IPFL00010). The PVDF membrane was incubated with blocking buffer (Rockland, Catalog # MB-070) at room temperature for one hr. The membrane was incubated with primary antibody at 4°C overnight. The following primary antibodies were used in the study: MCU, MCUB, MICU1, MICU2, VDAC, ETC respiratory chain complexes, anti-APP N-terminal raised against amino acids 66–81 for total APP 22C11, BACE1, ADAM-10, PS1, nicastrin, APH1, total tau HT7, phospho-tau (pThr231, AT180), phospho-Tau (Ser202, Thr205, AT8), phospho-tau (pThr181, AT270), phospho-tau (pS396, PHF13), beta-Tubulin, SYP dilution, PSD-95 dilution, GFAP. After incubation with primary antibody, the membrane was washed three times with TBS-T (TBS containing 0.1% Tween 20) for 10 min each and then incubated with specific secondary antibody for 1hr at room temperature. Licor IR secondary antibodies were used at dilutions 1:10,000. All blots were imaged on a Licor Odyssey system. All full-length western blots are available in Supplementary Figure 6.

Memory tests

Mice at 6, 9, 12, and 15 months of age were assessed for spatial working memory in the Y-maze and hippocampal-dependent associative learning memory in fear conditioning assay.

Y-maze

We assessed spatial working memory by measuring spontaneous alternation in a Y-maze. In this assay, test animals were placed in the center of the Y-shaped maze (San Diego Instruments, 32 cm (long) 610 cm (wide) with 26-cm walls) for 5 min and the total number of arms entered, as well as the sequence of entries, were recorded. A spontaneous alternation was defined when a mouse enters a different arm of the maze in each of three consecutive arm entries (i.e., 1, 2, 3, or 2, 3, 1, or 3,1,2). Spontaneous alternation % was then calculated with the following formula: total alternation number/total number of entries-2 × 100. Prior to initial use, the arms of the maze were clearly designated as '1', '2' & '3', and the maze was always wiped clean with 70% ethanol, followed by water between each animal.

Fear conditioning

The fear-conditioning was performed in a fear-conditioning apparatus (StartFear, Panlab Harvard Apparatus, 25 cm height × 30 cm width × 25 cm depth). The chamber was consisted of black methacrylate walls, a transparent front door, a light, a speaker, and a removable grid stainless-steel rod floor (3.2 mm diameter, 4.7 mm apart) through which a foot shock was administered. Automated fear conditioning FREEZING software was used to record and analyze signals generated by the animal movement throughout the procedure. Before each test, the chamber was cleaned with 70% ethanol, followed by water. In this test, mice were trained and tested on two consecutive days. On day 1 (training phase), each mouse was placed in the chamber and underwent three cycles of 30 s of sound and 10 s of electric shock (1.5 mA) within a 6-minute time interval. On day 2, the mouse returned to the same chamber without receiving electric shock or hearing the sound (contextual recall), and freezing behavior was recorded for 5 min. Two hours later, the animal spent 6 min in the same chamber but in an altered chamber environment, for example, different flooring, walls, smells, and lighting, and heard the cued sound for 30 s (cued recall), but without a foot shock. Freezing % was equal to (freezing time/total time) × 100%. All procedures were coordinated via PACKWIN (Panlab, Harvard

Apparatus, USA) on a computer connected to the device, and data analysis was performed using the same software.

Assessment of reactive oxygen species production. We employed Dihydroethidium (DHE) staining for in vivo detection of superoxide levels, as described (29). In brief, we freshly prepared cortical, and hippocampal slices from mice brains and stained them with 20 μM DHE for 30 min at 37°C and imaged at 518/excitation and 606/ emission on a Carl Zeiss 710 confocal microscope. To examine the total cellular ROS, cells from all groups were loaded with 5 μM CellROX Green Reagent for 30 min at 37 °C. CellROX exhibits a strong fluorogenic signal upon oxidation. The fluorescence at 485/excitation and 520/ emission was measured using a Tecan Infinite M1000 Pro plate reader. Next, we measured mitochondrial superoxide production using MitoSOX staining. Cells were loaded with 10 μM MitoSOX Red for 45 min at 37 °C and imaged at 490/20 excitation and 585/40 emission on Carl Zeiss 510 confocal microscope. All images were quantified for fluorescent optical density using ImageJ.

Membrane Rupture and cell viability assay. We used SYTOX Green nucleic acid stain to examine membrane rupture and Cell Titer Blue to evaluate cell viability. SYTOX Green is a membrane-impermeable fluorescent stain that becomes permeable with compromised plasma membranes and intercalates in DNA and increases fluorescence. The Cell Titer Blue assay uses the indicator dye resazurin to measure cells' metabolic capacity that an indicator of cell viability. In a 96-well plate, equal numbers of cells from all groups were treated with Ionomycin (2–10 μM) and an oxidizing agent tert-Butyl hydroperoxide solution (TBH: 10–50 μM) for 24 hrs. On the day of the experiment, SYTOX green dye was added to wells at 1 μM final concentration for 15 min at 37 °C. Fluorescence was measured using a Tecan Infinite M1000 Pro plate reader at 504/ excitation and 523/ emission. To measure the number of viable cells, Cell Titer Blue Reagent (10μl/well in 96 well plates) was added directly to each well and incubated at 37°C for 2 hrs. Fluorescence was measured using a Tecan Infinite M1000 Pro plate reader at 560/

excitation and 590/ emission. Data were normalized to vehicle control to avoid any differences in cell numbers between the groups.

Evaluation of $_{m}Ca^{2+}$ retention capacity and content. Assessment of $_{m}Ca^{2+}$ uptake and content were performed as reported previously (29). Cells (2×10^{6}) from all groups were washed in Ca^{2+} -free DPBS and resuspended in an intracellular-like medium (120 mM KCl, 10 mM NaCl, 1 mM KH2PO4, 20 mM HEPES-Tris) containing thapsigargin (3 μM) to block the SERCA pump, digitonin (80-μg/ml), protease inhibitor, and succinate (10 μM) at pH 7.2. All solutions were cleared with Chelex 100 to remove trace Ca^{2+}. To measure $_{m}Ca^{2+}$ uptake, cells were gently stirred and loaded with the ratiometric reporters Fura-FF at concentration of 1 μM to monitor extra-mitochondrial Ca^{2+}. To monitor mitochondrial membrane potential (Δψ), JC1 was added at 20 s. Fluorescence signals were monitored at 340- and 380-nm excitation /510-nm emission for Fura-FF to calculate ratiometric changes and at 490 nm excitation/535 nm emission for the monomer 570 nm excitation/595 nm emission for the J-aggregate of JC-1. After acquiring baseline recordings, a 10 μM Ca^{2+} bolus was added at 400 s. Clearance of extra-mitochondrial Ca^{2+} was representative of $_{m}Ca^{2+}$ uptake. At 550s, a protonophore, 10 μM FCCP (a protonophore) was added to uncouple the Δψm and release matrix-free-Ca^{2+}. All experiments (three replicates) were conducted at 37°C and recorded on a PTI spectrofluorometer (Delta RAM, Photon Technology Int.). The $_{m}Ca^{2+}$ uptake rate was recorded over 50s post Ca^{2+} bolus. To evaluate $_{m}Ca^{2+}$ content, permeabilized cells from all the groups were loaded with Fura-2 for ratiometric monitoring of extra-mitochondrial Ca^{2+} using a fluorescent spectrofluorometer. Upon reaching a steady-state recording, FCCP was used to collapse ΔΨ and liberate all matrix-free-Ca^{2+}. To assess $_{m}Ca^{2+}$ retention capacity in vivo, we next isolated mitochondria from frontal cortex of mice and performed Calcium Green 5 n to monitor extra-mitochondrial Ca^{2+} as described previously (29). After baseline recordings at 400 s, 5 μM- repetitive Ca^{2+} boluses were added and fluorescent signal at (488Ex/530Em) was measured using plate reader.

Transmission electron microscopy. Mice were anesthetized and perfused with PBS for 5 min and then with a fixative solution of 2% paraformaldehyde/2% glutaraldehyde in 0.1M sodium cacodylate buffer. After dissection, intact brain was placed in a fresh solution of the fixative overnight at 4 °C under agitation. Coronal sections (100-200um) were cut with the vibratome and then processed the tissue slices and embed in epoxy resin over a period of 48 h. The areas of interest (cortex, three blocks per mouse) were cut out of the slices with Reichert-Jung Ultracut E ultramicrotome and mounted for ultrathin sectioning for the TEM on Athene 200 mesh thin bar formvar-carbon coated copper grids. Sections were visualized with a Zeiss Libra 120 transmission electron microscope operating at 120 kV, using a Gatan Ultrascan 1000 CCD camera. We used ImageJ software to analyze mitochondria ultrastructure and mitochondrial shape descriptors (area, perimeter, circularity, Feret's diameter, aspect ratio). Minimum of 200 mitochondria were analyzed per mouse, n = 4 mice per group.

Quantification of mitochondrial copy number. The genomic DNA was isolated from mice brain cortex tissue using the DNeasy blood and tissue kit (Qiagen 69504) according to manufacturer's instructions. Quantification of mtDNA copy number was performed via quantitative PCR (qPCR) using the primers mitochondrial COXII gene and nuclear β-Globin (29).

Statistics. Prism 6.0 Graph Pad software was used for statistical analysis and to generate plots. All results are shown as mean ± SEM. All experiments were repeated at least three times and measurements were taken on distinct samples. Individual data points mean and s.e.m. were displayed in the figures. Where appropriate column analyses were performed using an unpaired, two-tailed *t* test (for two groups) or one-way ANOVA with Bonferroni correction (for groups of three or more). For grouped analyses either multiple unpaired t-test with correction for multiple comparisons using the Holm–Sidak method or where appropriate two-way ANOVA with Tukey post hoc analysis was performed. The specific statistical tests for each experiment are

indicated throughout the manuscript. Results were significant if p values < 0.05 (95% confidence interval).

Study approval. Animal studies were approved by Temple University's IACUC and followed AAALAC guidelines.

Author contributions. J.W.E. conceived the project; J.W.E. and P.J. contributed to study design, data analysis and writing the paper; P.J., D.T., D.K., M.T., A.N.H. and S.K performed experiments, data collection and interpretation, P.J. and D.K. performed histology and memory test experiments, D.T. and M.T. assisted with calcium content and imaging assays; J.W.E., and J.G. edited the manuscript and provided expertise with data interpretation.

Acknowledgments. We thank Trevor Tierney and Oniel Salik for technical assistance in the Elrod Lab. Support for this work was provided by grants from the NIH: R01NS121379**,** R01HL136954, R01HL142271, 3R01HL123966-05S1, P01HL147841, P01HL134608; AHA: 20EIA35320226, and Pennsylvania Dept. of Health CURE Award (420792) to J.W.E.; NIH K99AG065445 to P.J., NIH K99DK120876 to D.T. and NIH F32HL151146 to J.F.G.

REFERENCES

1. Du H, Guo L, Fang F, Chen D, Sosunov AA, McKhann GM, et al. Cyclophilin D deficiency attenuates mitochondrial and neuronal perturbation and ameliorates learning and memory in Alzheimer's disease. *Nat Med.* 2008;14(10):1097-105.
2. Gillardon F, Rist W, Kussmaul L, Vogel J, Berg M, Danzer K, et al. Proteomic and functional alterations in brain mitochondria from Tg2576 mice occur before amyloid plaque deposition. *Proteomics.* 2007;7(4):605-16.
3. Rossi A, Rigotto G, Valente G, Giorgio V, Basso E, Filadi R, et al. Defective Mitochondrial Pyruvate Flux Affects Cell Bioenergetics in Alzheimer's Disease-Related Models. *Cell Rep.* 2020;30(7):2332-48 e10.
4. Begley JG, Duan W, Chan S, Duff K, and Mattson MP. Altered calcium homeostasis and mitochondrial dysfunction in cortical synaptic compartments of presenilin-1 mutant mice. *J Neurochem.* 1999;72(3):1030-9.
5. Mattson MP, Cheng B, Davis D, Bryant K, Lieberburg I, and Rydel RE. beta-Amyloid peptides destabilize calcium homeostasis and render human cortical neurons vulnerable to excitotoxicity. *J Neurosci.* 1992;12(2):376-89.
6. Barrett EF, Barrett JN, and David G. Dysfunctional mitochondrial Ca(2+) handling in mutant SOD1 mouse models of fALS: integration of findings from motor neuron somata and motor terminals. *Front Cell Neurosci.* 2014;8:184.
7. Kipanyula MJ, Contreras L, Zampese E, Lazzari C, Wong AK, Pizzo P, et al. Ca2+ dysregulation in neurons from transgenic mice expressing mutant presenilin 2. *Aging Cell.* 2012;11(5):885-93.
8. Verma M, Callio J, Otero PA, Sekler I, Wills ZP, and Chu CT. Mitochondrial Calcium Dysregulation Contributes to Dendrite Degeneration Mediated by PD/LBD-Associated LRRK2 Mutants. *J Neurosci.* 2017;37(46):11151-65.

9. Dreses-Werringloer U, Lambert JC, Vingtdeux V, Zhao H, Vais H, Siebert A, et al. A polymorphism in CALHM1 influences Ca2+ homeostasis, Abeta levels, and Alzheimer's disease risk. *Cell.* 2008;133(7):1149-61.

10. Chang EH, Savage MJ, Flood DG, Thomas JM, Levy RB, Mahadomrongkul V, et al. AMPA receptor downscaling at the onset of Alzheimer's disease pathology in double knockin mice. *Proc Natl Acad Sci U S A.* 2006;103(9):3410-5.

11. Tong BC, Lee CS, Cheng WH, Lai KO, Foskett JK, and Cheung KH. Familial Alzheimer's disease-associated presenilin 1 mutants promote gamma-secretase cleavage of STIM1 to impair store-operated Ca2+ entry. *Sci Signal.* 2016;9(444):ra89.

12. Paula-Lima AC, Adasme T, SanMartin C, Sebollela A, Hetz C, Carrasco MA, et al. Amyloid beta-peptide oligomers stimulate RyR-mediated Ca2+ release inducing mitochondrial fragmentation in hippocampal neurons and prevent RyR-mediated dendritic spine remodeling produced by BDNF. *Antioxid Redox Signal.* 2011;14(7):1209-23.

13. Ferreira IL, Ferreiro E, Schmidt J, Cardoso JM, Pereira CM, Carvalho AL, et al. Abeta and NMDAR activation cause mitochondrial dysfunction involving ER calcium release. *Neurobiol Aging.* 2015;36(2):680-92.

14. Area-Gomez E, de Groof A, Bonilla E, Montesinos J, Tanji K, Boldogh I, et al. A key role for MAM in mediating mitochondrial dysfunction in Alzheimer disease. *Cell Death Dis.* 2018;9(3):335.

15. Area-Gomez E, Del Carmen Lara Castillo M, Tambini MD, Guardia-Laguarta C, de Groof AJ, Madra M, et al. Upregulated function of mitochondria-associated ER membranes in Alzheimer disease. *EMBO J.* 2012;31(21):4106-23.

16. Calvo-Rodriguez M, Hernando-Perez E, Nunez L, and Villalobos C. Amyloid beta Oligomers Increase ER-Mitochondria Ca(2+) Cross Talk in Young Hippocampal Neurons

and Exacerbate Aging-Induced Intracellular Ca(2+) Remodeling. *Front Cell Neurosci.* 2019;13:22.

17. Lustbader JW, Cirilli M, Lin C, Xu HW, Takuma K, Wang N, et al. ABAD directly links Abeta to mitochondrial toxicity in Alzheimer's disease. *Science.* 2004;304(5669):448-52.

18. Lacampagne A, Liu X, Reiken S, Bussiere R, Meli AC, Lauritzen I, et al. Post-translational remodeling of ryanodine receptor induces calcium leak leading to Alzheimer's disease-like pathologies and cognitive deficits. *Acta Neuropathol.* 2017;134(5):749-67.

19. Cheung KH, Mei L, Mak DO, Hayashi I, Iwatsubo T, Kang DE, et al. Gain-of-function enhancement of IP3 receptor modal gating by familial Alzheimer's disease-linked presenilin mutants in human cells and mouse neurons. *Sci Signal.* 2010;3(114):ra22.

20. Cheung KH, Shineman D, Muller M, Cardenas C, Mei L, Yang J, et al. Mechanism of Ca2+ disruption in Alzheimer's disease by presenilin regulation of InsP3 receptor channel gating. *Neuron.* 2008;58(6):871-83.

21. Muller M, Cheung KH, and Foskett JK. Enhanced ROS generation mediated by Alzheimer's disease presenilin regulation of InsP3R Ca2+ signaling. *Antioxid Redox Signal.* 2011;14(7):1225-35.

22. Billups B, and Forsythe ID. Presynaptic mitochondrial calcium sequestration influences transmission at mammalian central synapses. *J Neurosci.* 2002;22(14):5840-7.

23. Cardenas C, Miller RA, Smith I, Bui T, Molgo J, Muller M, et al. Essential regulation of cell bioenergetics by constitutive InsP3 receptor Ca2+ transfer to mitochondria. *Cell.* 2010;142(2):270-83.

24. Denton RM, Randle PJ, and Martin BR. Stimulation by calcium ions of pyruvate dehydrogenase phosphate phosphatase. *Biochem J.* 1972;128(1):161-3.

25. Denton RM, Richards DA, and Chin JG. Calcium ions and the regulation of NAD+-linked isocitrate dehydrogenase from the mitochondria of rat heart and other tissues. *Biochem J.* 1978;176(3):899-906.

26. Szalai G, Krishnamurthy R, and Hajnoczky G. Apoptosis driven by IP(3)-linked mitochondrial calcium signals. *EMBO J.* 1999;18(22):6349-61.

27. Nakagawa T, Zhu H, Morishima N, Li E, Xu J, Yankner BA, et al. Caspase-12 mediates endoplasmic-reticulum-specific apoptosis and cytotoxicity by amyloid-beta. *Nature.* 2000;403(6765):98-103.

28. Luongo TS, Lambert JP, Yuan A, Zhang X, Gross P, Song J, et al. The Mitochondrial Calcium Uniporter Matches Energetic Supply with Cardiac Workload during Stress and Modulates Permeability Transition. *Cell Rep.* 2015;12(1):23-34.

29. Jadiya P, Kolmetzky DW, Tomar D, Di Meco A, Lombardi AA, Lambert JP, et al. Impaired mitochondrial calcium efflux contributes to disease progression in models of Alzheimer's disease. *Nat Commun.* 2019;10(1):3885.

30. Calvo-Rodriguez M, Hou SS, Snyder AC, Kharitonova EK, Russ AN, Das S, et al. Increased mitochondrial calcium levels associated with neuronal death in a mouse model of Alzheimer's disease. *Nature communications.* 2020;11(1):2146.

31. Kostic M, Ludtmann MH, Bading H, Hershfinkel M, Steer E, Chu CT, et al. PKA Phosphorylation of NCLX Reverses Mitochondrial Calcium Overload and Depolarization, Promoting Survival of PINK1-Deficient Dopaminergic Neurons. *Cell Rep.* 2015;13(2):376-86.

32. Logan CV, Szabadkai G, Sharpe JA, Parry DA, Torelli S, Childs AM, et al. Loss-of-function mutations in MICU1 cause a brain and muscle disorder linked to primary alterations in mitochondrial calcium signaling. *Nat Genet.* 2014;46(2):188-93.

33. Qiu J, Tan YW, Hagenston AM, Martel MA, Kneisel N, Skehel PA, et al. Mitochondrial calcium uniporter Mcu controls excitotoxicity and is transcriptionally repressed by neuroprotective nuclear calcium signals. *Nat Commun.* 2013;4:2034.

34. Granatiero V, Pacifici M, Raffaello A, De Stefani D, and Rizzuto R. Overexpression of Mitochondrial Calcium Uniporter Causes Neuronal Death. *Oxid Med Cell Longev.* 2019;2019:1681254.

35. Perez MJ, Ponce DP, Aranguiz A, Behrens MI, and Quintanilla RA. Mitochondrial permeability transition pore contributes to mitochondrial dysfunction in fibroblasts of patients with sporadic Alzheimer's disease. *Redox Biol.* 2018;19:290-300.

36. Sarasija S, Laboy JT, Ashkavand Z, Bonner J, Tang Y, and Norman KR. Presenilin mutations deregulate mitochondrial Ca(2+) homeostasis and metabolic activity causing neurodegeneration in Caenorhabditis elegans. *Elife.* 2018;7.

37. Stutzmann GE, Caccamo A, LaFerla FM, and Parker I. Dysregulated IP3 signaling in cortical neurons of knock-in mice expressing an Alzheimer's-linked mutation in presenilin1 results in exaggerated Ca2+ signals and altered membrane excitability. *J Neurosci.* 2004;24(2):508-13.

38. Baughman JM, Perocchi F, Girgis HS, Plovanich M, Belcher-Timme CA, Sancak Y, et al. Integrative genomics identifies MCU as an essential component of the mitochondrial calcium uniporter. *Nature.* 2011;476(7360):341-5.

39. De Stefani D, Raffaello A, Teardo E, Szabo I, and Rizzuto R. A forty-kilodalton protein of the inner membrane is the mitochondrial calcium uniporter. *Nature.* 2011;476(7360):336-40.

40. Tsien JZ, Chen DF, Gerber D, Tom C, Mercer EH, Anderson DJ, et al. Subregion- and cell type-restricted gene knockout in mouse brain. *Cell.* 1996;87(7):1317-26.

41. Oddo S, Caccamo A, Shepherd JD, Murphy MP, Golde TE, Kayed R, et al. Triple-transgenic model of Alzheimer's disease with plaques and tangles: intracellular Abeta and synaptic dysfunction. *Neuron.* 2003;39(3):409-21.

42. Curzon P, Rustay NR, and Browman KE. In: nd, and Buccafusco JJ eds. *Methods of Behavior Analysis in Neuroscience*. Boca Raton (FL); 2009.

43. Abeti R, and Abramov AY. Mitochondrial Ca(2+) in neurodegenerative disorders. *Pharmacological research.* 2015;99:377-81.

44. Berridge MJ. Calcium hypothesis of Alzheimer's disease. *Pflugers Archiv : European journal of physiology.* 2010;459(3):441-9.

45. Shilling D, Muller M, Takano H, Mak DO, Abel T, Coulter DA, et al. Suppression of InsP3 receptor-mediated Ca2+ signaling alleviates mutant presenilin-linked familial Alzheimer's disease pathogenesis. *J Neurosci.* 2014;34(20):6910-23.

46. Butterfield DA, and Boyd-Kimball D. Oxidative Stress, Amyloid-beta Peptide, and Altered Key Molecular Pathways in the Pathogenesis and Progression of Alzheimer's Disease. *J Alzheimers Dis.* 2018;62(3):1345-67.

47. Hong S, Beja-Glasser VF, Nfonoyim BM, Frouin A, Li S, Ramakrishnan S, et al. Complement and microglia mediate early synapse loss in Alzheimer mouse models. *Science.* 2016;352(6286):712-6.

48. Almeida CG, Tampellini D, Takahashi RH, Greengard P, Lin MT, Snyder EM, et al. Beta-amyloid accumulation in APP mutant neurons reduces PSD-95 and GluR1 in synapses. *Neurobiol Dis.* 2005;20(2):187-98.

49. Benarroch EE. Glutamatergic synaptic plasticity and dysfunction in Alzheimer disease: Emerging mechanisms. *Neurology.* 2018;91(3):125-32.

50. Jackson J, Jambrina E, Li J, Marston H, Menzies F, Phillips K, et al. Targeting the Synapse in Alzheimer's Disease. *Front Neurosci.* 2019;13:735.

51. Tarsa L, and Goda Y. Synaptophysin regulates activity-dependent synapse formation in cultured hippocampal neurons. *Proc Natl Acad Sci U S A.* 2002;99(2):1012-6.

52. El-Husseini AE, Schnell E, Chetkovich DM, Nicoll RA, and Bredt DS. PSD-95 involvement in maturation of excitatory synapses. *Science.* 2000;290(5495):1364-8.

53. Migaud M, Charlesworth P, Dempster M, Webster LC, Watabe AM, Makhinson M, et al. Enhanced long-term potentiation and impaired learning in mice with mutant postsynaptic density-95 protein. *Nature.* 1998;396(6710):433-9.

54. Kim E, Cho KO, Rothschild A, and Sheng M. Heteromultimerization and NMDA receptor-clustering activity of Chapsyn-110, a member of the PSD-95 family of proteins. *Neuron.* 1996;17(1):103-13.

55. Habib N, McCabe C, Medina S, Varshavsky M, Kitsberg D, Dvir-Szternfeld R, et al. Disease-associated astrocytes in Alzheimer's disease and aging. *Nat Neurosci.* 2020;23(6):701-6.

56. Park JS, Kam TI, Lee S, Park H, Oh Y, Kwon SH, et al. Blocking microglial activation of reactive astrocytes is neuroprotective in models of Alzheimer's disease. *Acta Neuropathol Commun.* 2021;9(1):78.

57. Caruso D, Barron AM, Brown MA, Abbiati F, Carrero P, Pike CJ, et al. Age-related changes in neuroactive steroid levels in 3xTg-AD mice. *Neurobiol Aging.* 2013;34(4):1080-9.

58. Thinakaran G, Teplow DB, Siman R, Greenberg B, and Sisodia SS. Metabolism of the "Swedish" amyloid precursor protein variant in neuro2a (N2a) cells. Evidence that cleavage at the "beta-secretase" site occurs in the golgi apparatus. *J Biol Chem.* 1996;271(16):9390-7.

59. Mallilankaraman K, Doonan P, Cardenas C, Chandramoorthy HC, Muller M, Miller R, et al. MICU1 is an essential gatekeeper for MCU-mediated mitochondrial Ca(2+) uptake that regulates cell survival. *Cell.* 2012;151(3):630-44.

60. Perocchi F, Gohil VM, Girgis HS, Bao XR, McCombs JE, Palmer AE, et al. MICU1 encodes a mitochondrial EF hand protein required for Ca(2+) uptake. *Nature.* 2010;467(7313):291-6.

61. Plovanich M, Bogorad RL, Sancak Y, Kamer KJ, Strittmatter L, Li AA, et al. MICU2, a paralog of MICU1, resides within the mitochondrial uniporter complex to regulate calcium handling. *PLoS One.* 2013;8(2):e55785.

62. Raffaello A, De Stefani D, Sabbadin D, Teardo E, Merli G, Picard A, et al. The mitochondrial calcium uniporter is a multimer that can include a dominant-negative pore-forming subunit. *The EMBO journal.* 2013;32(17):2362-76.

63. Gandhi S, Wood-Kaczmar A, Yao Z, Plun-Favreau H, Deas E, Klupsch K, et al. PINK1-associated Parkinson's disease is caused by neuronal vulnerability to calcium-induced cell death. *Mol Cell.* 2009;33(5):627-38.

64. Luongo TS, Lambert JP, Gross P, Nwokedi M, Lombardi AA, Shanmughapriya S, et al. The mitochondrial Na(+)/Ca(2+) exchanger is essential for Ca(2+) homeostasis and viability. *Nature.* 2017;545(7652):93-7.

65. Fan MM, and Raymond LA. N-methyl-D-aspartate (NMDA) receptor function and excitotoxicity in Huntington's disease. *Prog Neurobiol.* 2007;81(5-6):272-93.

66. Lau A, and Tymianski M. Glutamate receptors, neurotoxicity and neurodegeneration. *Pflugers Arch.* 2010;460(2):525-42.

67. Wu HY, Tomizawa K, Oda Y, Wei FY, Lu YF, Matsushita M, et al. Critical role of calpain-mediated cleavage of calcineurin in excitotoxic neurodegeneration. *J Biol Chem.* 2004;279(6):4929-40.

68. Soman S, Keatinge M, Moein M, Da Costa M, Mortiboys H, Skupin A, et al. Inhibition of the mitochondrial calcium uniporter rescues dopaminergic neurons in pink1(-/-) zebrafish. *Eur J Neurosci.* 2017;45(4):528-35.

69. Soman SK, Bazala M, Keatinge M, Bandmann O, and Kuznicki J. Restriction of mitochondrial calcium overload by mcu inactivation renders a neuroprotective effect in zebrafish models of Parkinson's disease. *Biol Open.* 2019;8(10).

70. Zampese E, Fasolato C, Kipanyula MJ, Bortolozzi M, Pozzan T, and Pizzo P. Presenilin 2 modulates endoplasmic reticulum (ER)-mitochondria interactions and Ca2+ cross-talk. *Proc Natl Acad Sci U S A.* 2011;108(7):2777-82.

71. Orr AL, Kim C, Jimenez-Morales D, Newton BW, Johnson JR, Krogan NJ, et al. Neuronal Apolipoprotein E4 Expression Results in Proteome-Wide Alterations and Compromises Bioenergetic Capacity by Disrupting Mitochondrial Function. *J Alzheimers Dis.* 2019;68(3):991-1011.

72. Hansson CA, Frykman S, Farmery MR, Tjernberg LO, Nilsberth C, Pursglove SE, et al. Nicastrin, presenilin, APH-1, and PEN-2 form active gamma-secretase complexes in mitochondria. *J Biol Chem.* 2004;279(49):51654-60.

73. Del Prete D, Suski JM, Oules B, Debayle D, Gay AS, Lacas-Gervais S, et al. Localization and Processing of the Amyloid-beta Protein Precursor in Mitochondria-Associated Membranes. *J Alzheimers Dis.* 2017;55(4):1549-70.

74. Manczak M, Anekonda TS, Henson E, Park BS, Quinn J, and Reddy PH. Mitochondria are a direct site of A beta accumulation in Alzheimer's disease neurons: implications for free radical generation and oxidative damage in disease progression. *Hum Mol Genet.* 2006;15(9):1437-49.

75. Sorrentino V, Romani M, Mouchiroud L, Beck JS, Zhang H, D'Amico D, et al. Enhancing mitochondrial proteostasis reduces amyloid-beta proteotoxicity. *Nature.* 2017;552(7684):187-93.

76. Fonseca AC, Moreira PI, Oliveira CR, Cardoso SM, Pinton P, and Pereira CF. Amyloid-beta disrupts calcium and redox homeostasis in brain endothelial cells. *Mol Neurobiol.* 2015;51(2):610-22.

77. Sanz-Blasco S, Valero RA, Rodriguez-Crespo I, Villalobos C, and Nunez L. Mitochondrial Ca2+ overload underlies Abeta oligomers neurotoxicity providing an unexpected mechanism of neuroprotection by NSAIDs. *PLoS One.* 2008;3(7):e2718.

78. Calvo-Rodriguez M, Garcia-Durillo M, Villalobos C, and Nunez L. Aging Enables Ca2+ Overload and Apoptosis Induced by Amyloid-beta Oligomers in Rat Hippocampal Neurons: Neuroprotection by Non-Steroidal Anti-Inflammatory Drugs and R-Flurbiprofen in Aging Neurons. *J Alzheimers Dis.* 2016;54(1):207-21.

79. Cieri D, Vicario M, Vallese F, D'Orsi B, Berto P, Grinzato A, et al. Tau localises within mitochondrial sub-compartments and its caspase cleavage affects ER-mitochondria interactions and cellular Ca(2+) handling. *Biochim Biophys Acta Mol Basis Dis.* 2018;1864(10):3247-56.

80. Jo DG, Arumugam TV, Woo HN, Park JS, Tang SC, Mughal M, et al. Evidence that gamma-secretase mediates oxidative stress-induced beta-secretase expression in Alzheimer's disease. *Neurobiol Aging.* 2010;31(6):917-25.

81. Gabuzda D, Busciglio J, Chen LB, Matsudaira P, and Yankner BA. Inhibition of energy metabolism alters the processing of amyloid precursor protein and induces a potentially amyloidogenic derivative. *J Biol Chem.* 1994;269(18):13623-8.

82. Rhein V, Song X, Wiesner A, Ittner LM, Baysang G, Meier F, et al. Amyloid-beta and tau synergistically impair the oxidative phosphorylation system in triple transgenic Alzheimer's disease mice. *Proc Natl Acad Sci U S A.* 2009;106(47):20057-62.

83. Petersen A, Castilho RF, Hansson O, Wieloch T, and Brundin P. Oxidative stress, mitochondrial permeability transition and activation of caspases in calcium ionophore A23187-induced death of cultured striatal neurons. *Brain Res.* 2000;857(1-2):20-9.

84. Starkov AA, Chinopoulos C, and Fiskum G. Mitochondrial calcium and oxidative stress as mediators of ischemic brain injury. *Cell Calcium.* 2004;36(3-4):257-64.

85. Stout AK, Raphael HM, Kanterewicz BI, Klann E, and Reynolds IJ. Glutamate-induced neuron death requires mitochondrial calcium uptake. *Nat Neurosci.* 1998;1(5):366-73.

86. Xie N, Wu C, Wang C, Cheng X, Zhang L, Zhang H, et al. Inhibition of the mitochondrial calcium uniporter inhibits Abeta-induced apoptosis by reducing reactive oxygen species-mediated endoplasmic reticulum stress in cultured microglia. *Brain Res.* 2017;1676:100-6.

87. Liao Y, Hao Y, Chen H, He Q, Yuan Z, and Cheng J. Mitochondrial calcium uniporter protein MCU is involved in oxidative stress-induced cell death. *Protein Cell.* 2015;6(6):434-42.

88. Gylys KH, Fein JA, Yang F, Wiley DJ, Miller CA, and Cole GM. Synaptic changes in Alzheimer's disease: increased amyloid-beta and gliosis in surviving terminals is accompanied by decreased PSD-95 fluorescence. *Am J Pathol.* 2004;165(5):1809-17.

89. Oyarzabal A, and Marin-Valencia I. Synaptic energy metabolism and neuronal excitability, in sickness and health. *J Inherit Metab Dis.* 2019;42(2):220-36.

90. Vergara RC, Jaramillo-Riveri S, Luarte A, Moenne-Loccoz C, Fuentes R, Couve A, et al. The Energy Homeostasis Principle: Neuronal Energy Regulation Drives Local Network Dynamics Generating Behavior. *Front Comput Neurosci.* 2019;13:49.

91. Harris JJ, Jolivet R, and Attwell D. Synaptic energy use and supply. *Neuron.* 2012;75(5):762-77.

92. Li S, Xiong GJ, Huang N, and Sheng ZH. The cross-talk of energy sensing and mitochondrial anchoring sustains synaptic efficacy by maintaining presynaptic metabolism. *Nat Metab.* 2020;2(10):1077-95.

93. Denton RM. Regulation of mitochondrial dehydrogenases by calcium ions. *Biochim Biophys Acta.* 2009;1787(11):1309-16.

94. Nichols BJ, and Denton RM. Towards the molecular basis for the regulation of mitochondrial dehydrogenases by calcium ions. *Mol Cell Biochem.* 1995;149-150:203-12.

95. Panel M, Ghaleh B, and Morin D. Mitochondria and aging: A role for the mitochondrial transition pore? *Aging Cell.* 2018;17(4):e12793.

96. Evangelopoulos ME, Weis J, and Kruttgen A. Signalling pathways leading to neuroblastoma differentiation after serum withdrawal: HDL blocks neuroblastoma differentiation by inhibition of EGFR. *Oncogene.* 2005;24(20):3309-18.

FIGURE LEGENDS

Figure 1. Loss of neuronal $_{m}Ca^{2+}$ uptake improves AD-associated cognitive deficits. A Schematic of *Mcu* knockout 3xTg-AD mutant mouse gene-targeting strategy. **B** Western blots for MCU expression and proteins associated with $_{m}Ca^{2+}$ exchange in tissue isolated from the cortex of 2 months old 3xTg-AD x *Mcu*$^{fl/fl}$ x Camk2a-Cre mice compared to age-matched control. MCU, mitochondrial calcium uniporter; MCUB, mitochondrial calcium uniporter β subunit; MICU1, mitochondrial calcium uptake 1; MICU2, mitochondrial calcium uptake 2; MICU3, mitochondrial calcium uptake 3; EMRE, Essential MCU Regulator; NCLX, Mitochondrial Na+/Ca2+ Exchanger. VDAC, Voltage-dependent anion channel served as mitochondrial loading controls. **C** Western blots for MCU expression and proteins associated with $_{m}Ca^{2+}$ exchange in tissue isolated from the cortex of 12 months old 3xTg-AD x *Mcu*$^{fl/fl}$ x Camk2a-Cre mutant mice compared to age-matched control. **D** Representative traces for $_{m}Ca^{2+}$ retention capacity (CRC). **E** Percent change in CRC of 3xTg-AD × Camk2a-Cre and 3xTg-AD × *Mcu*$^{fl/fl}$ × Camk2a-Cre vs. Camk2a-Cre control. **F** $_{m}Ca^{2+}$ uptake rate expressed as fold-change vs. Camk2a-Cre con. calculated after first 5-μm Ca^{2+} bolus. **G, H** Y-maze spontaneous alternation test. **G** Percentage of spontaneous alternation. **H** Total number of arm entries. **I–K** Fear-conditioning test. **I** Freezing responses in the training phase. **J** Contextual recall freezing responses, **K** Cued recall freezing responses. n = individual dots shown for each group in all graphs. All data presented as mean ± SEM; ****$p < 0.001$, **$p < 0.01$, *$p < 0.05$; one-way ANOVA with Sidak's multiple comparisons test.

Figure 2. Genetic ablation of neuronal $_{m}Ca^{2+}$ uptake attenuates Aβ accumulation in 3xTg-AD mice. A, B Soluble and insoluble $A\beta_{1–40}$ and $A\beta_{1–42}$ levels in the cortex of 15 months old mice, measured by sandwich ELISA. **C, D** Soluble and insoluble $A\beta_{1–40}$ and $A\beta_{1–42}$ levels in the hippocampus of 15 months old mice, measured by sandwich ELISA. n = individual dots shown for each group in all graphs. **E** Representative immunohistochemical staining for 4G8-reactive β-amyloid; 4× scale bar = 100 μM, 40× scale bar = 50 μM. **F** Quantification of the integrated

optical density area for Aβ immunoreactivity, n = 4 for all groups. **G** Western blots of full-length APP, ADAM-10, BACE1, PS1, Nicastrin, APH, and tubulin (loading control) for cortex homogenate of 15 months old mice, n = 3 for all groups. All data presented as mean ± SEM; ****p < 0.001, **p < 0.01, *p < 0.05; one-way ANOVA with Sidak's multiple comparisons test.

Figure 3. Loss of neuronal MCU expression decreases tau pathology. A Representative western blot of soluble and insoluble total tau (HT7), phosphorylated tau at residues S202/T205 (AT8), T231/S235 (AT180), T181 (AT270), and S396 (PHF13) in cortex homogenate of 15 months old mice, n = 3 for all groups. **B-E** Densitometric analysis of Western blots shown in Figure 3A and Figure S3A, expressed as fold-change vs. Camk2a-Cre con. corrected to a loading control tubulin. Quantification is the sum of all replicates, n=6. **F** Representative immunohistochemical staining for total tau (HT7), phospho-tau S202/T205 (AT8), and phospho-tau T231/S235 (AT180) in the hippocampus of mice; scale bar = 50 μM. **G, H** Quantification of the integrated optical density area of AT8 and AT180 immunoreactivity, n = 4 for all groups. All data presented as mean ± SEM; ****p < 0.001, **p < 0.01, *p < 0.05; one-way ANOVA with Sidak's multiple comparisons test.

Figure 4. Neuronal deletion of *Mcu* reduces oxidative stress, improves synaptic integrity, and reduces neuroinflammation. A DHE staining for ex vivo detection of superoxide production in freshly prepared cortical and hippocampal sections from 15 months old mice. **B, C** DHE fluorescent intensity, percent change vs. 3xTg-AD × Camk2a-Cre controls. n = 4 for all groups. **D** Representative image of 4-HNE immunohistochemistry in cortex and hippocampus to detect lipid peroxidation in 15 months old mice. **E, F** Percent change in 4-HNE-integrated optical density area corrected to 3xTg-AD × Camk2a-Cre controls. n = 4 for all groups. **G, H** Western blots for SYP, PSD-95, GFAP and IBA1 expression in tissue isolated from the cortex of 15 months old mice, n = 3 for all groups. All data presented as mean ± SEM; ****p < 0.001, **p < 0.01, *p < 0.05; one-way ANOVA with Sidak's multiple comparisons test.

Figure 5. Loss of $_mCa^{2+}$ uptake prevents AD-associated mitochondrial dysfunction. An Experimental protocol timeline for generation of stable *Mcu* knockdown N2a/APPswe cells. **B** Western blots for MCU expression and proteins associated with $_mCa^{2+}$ exchange in N2a and APPswe cells transduced with lentivirus encoding shRNA targeting *Mcu.* **C** MCU protein expression expressed as fold-change vs. N2a Scr-shRNA con. corrected to a mitochondrial loading control VDAC. **D** Representative recordings of $_mCa^{2+}$ uptake. **E** Percent change in $_mCa^{2+}$ uptake. **F** Representative traces for basal $_mCa^{2+}$ content, n = 3. **G** Quantification of $_mCa^{2+}$ content. **H** Quantification of CellRox green fluorescent intensity (total cellular ROS production); fold change vs. N2a Scr-shRNA controls. **I** Quantification of MitoSOX fluorescent intensity; fold change vs. N2a Scr-shRNA controls. All data presented as mean ± SEM; ****$p < 0.001$, **$p < 0.01$, *$p < 0.05$; one-way ANOVA with Sidak's multiple comparisons test. **J-K** Assessment for plasma membrane rupture, using Sytox Green, after treatment with: **J** Ionomycin (Ca^{2+} ionophore, 2–10 μM), **K** tert-Butyl hydroperoxide (TBH, oxidizing agent, 10–50 μM).
n = individual dots shown for each group in all graphs. All data presented as mean ± SEM; ****$p < 0.001$, **$p < 0.01$, *$p < 0.05$; two-way ANOVA with Sidak's multiple comparisons test.

Declaration of Interests

The authors declare no competing financial interests. Readers are welcome to comment on the online version of the paper. Correspondence and requests for materials should be addressed to J.W.E. (elrod@temple.edu).

Supplemental material

Supplementary information includes supplementary figures and can be found online with this article.

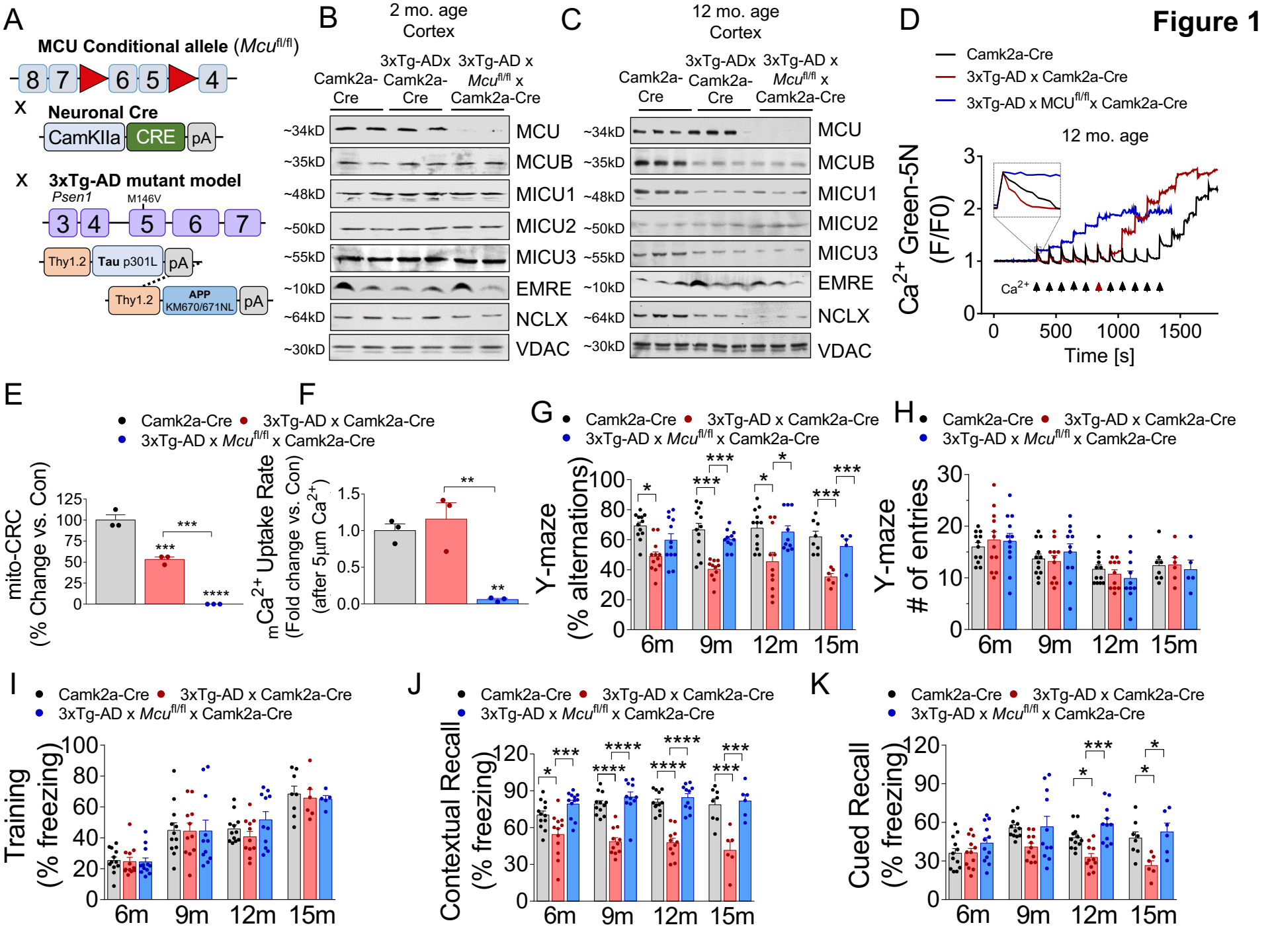

Figure 1
A
MCU Conditional allele (Mcu^fl/fl)
8 7 6 5 4
X Neuronal Cre
CamKIIa CRE pA
X 3xTg-AD mutant model
Psen1 M146V
3 4 5 6 7
Thy1.2 Tau p301L pA
Thy1.2 APP KM670/671NL pA
B
2 mo. age Cortex
Camk2a-Cre
3xTg-ADx Camk2a-Cre
3xTg-AD x Mcu^fl/fl x Camk2a-Cre
~34kD MCU
~35kD MCUB
~48kD MICU1
~50kD MICU2
~55kD MICU3
~10kD EMRE
~64kD NCLX
~30kD VDAC
C
12 mo. age Cortex
D
Camk2a-Cre
3xTg-AD x Camk2a-Cre
3xTg-AD x MCU^fl/fl x Camk2a-Cre
12 mo. age
Ca2+ Green-5N (F/F0)
Ca2+
Time [s]
E
mito-CRC (% Change vs. Con)
F
mCa2+ Uptake Rate (Fold change vs. Con) (after 5μm Ca2+)
G
Y-maze (% alternations)
H
Y-maze # of entries
I
Training (% freezing)
J
Contextual Recall (% freezing)
K
Cued Recall (% freezing)
6m 9m 12m 15m

Figure 2

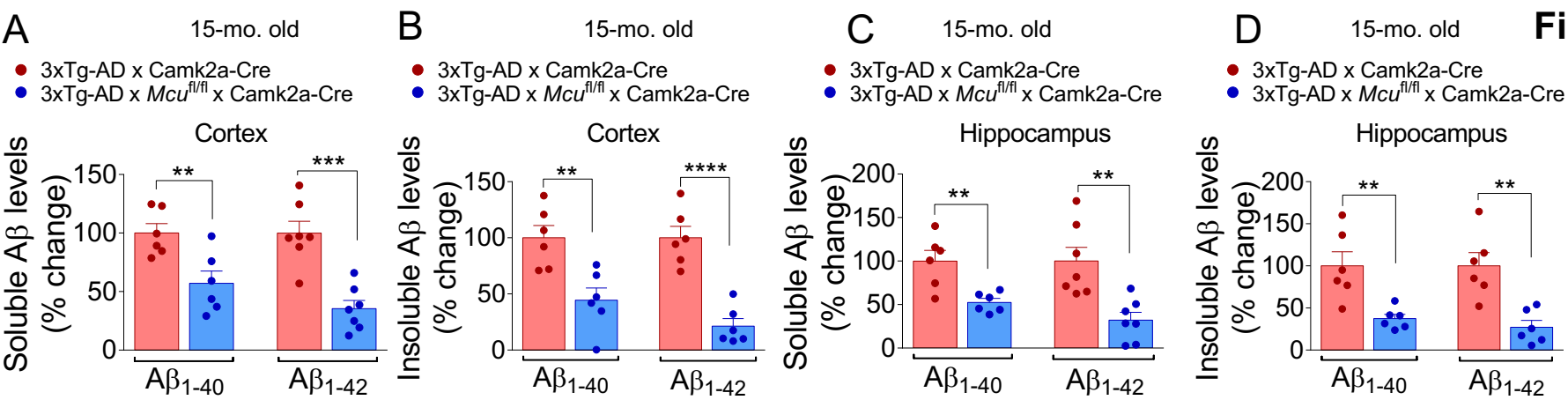
A
15-mo. old
3xTg-AD x Camk2a-Cre
3xTg-AD x Mcu fl/fl x Camk2a-Cre
Cortex
Soluble Aβ levels (% change)
150
100
50
0
**
***
Aβ1-40
Aβ1-42
B
15-mo. old
3xTg-AD x Camk2a-Cre
3xTg-AD x Mcu fl/fl x Camk2a-Cre
Cortex
Insoluble Aβ levels (% change)
150
100
50
0
**
****
Aβ1-40
Aβ1-42
C
15-mo. old
3xTg-AD x Camk2a-Cre
3xTg-AD x Mcu fl/fl x Camk2a-Cre
Hippocampus
Soluble Aβ levels (% change)
200
150
100
50
0
**
**
Aβ1-40
Aβ1-42
D
15-mo. old
3xTg-AD x Camk2a-Cre
3xTg-AD x Mcu fl/fl x Camk2a-Cre
Hippocampus
Insoluble Aβ levels (% change)
200
150
100
50
0
**
**
Aβ1-40
Aβ1-42

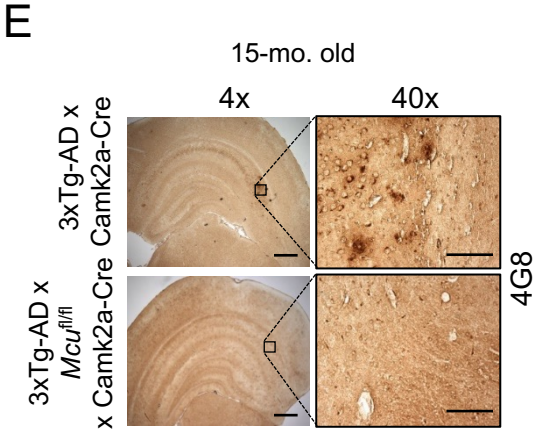
E
15-mo. old
4x
40x
3xTg-AD x Camk2a-Cre
3xTg-AD x Mcu fl/fl x Camk2a-Cre
4G8

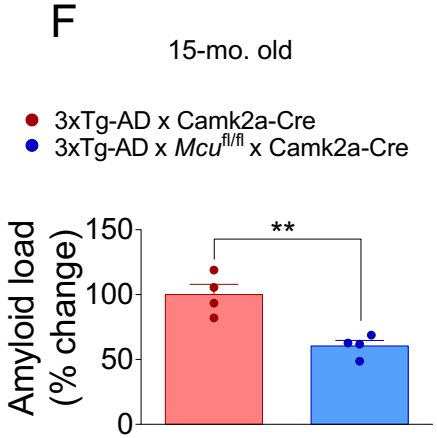
F
15-mo. old
3xTg-AD x Camk2a-Cre
3xTg-AD x Mcu fl/fl x Camk2a-Cre
Amyloid load (% change)
150
100
50
0
**

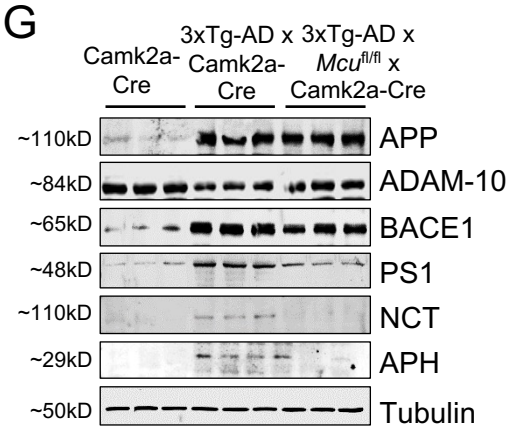
G
Camk2a-Cre
3xTg-AD x Camk2a-Cre
3xTg-AD x Mcu fl/fl x Camk2a-Cre
~110kD
APP
~84kD
ADAM-10
~65kD
BACE1
~48kD
PS1
~110kD
NCT
~29kD
APH
~50kD
Tubulin

Figure 3

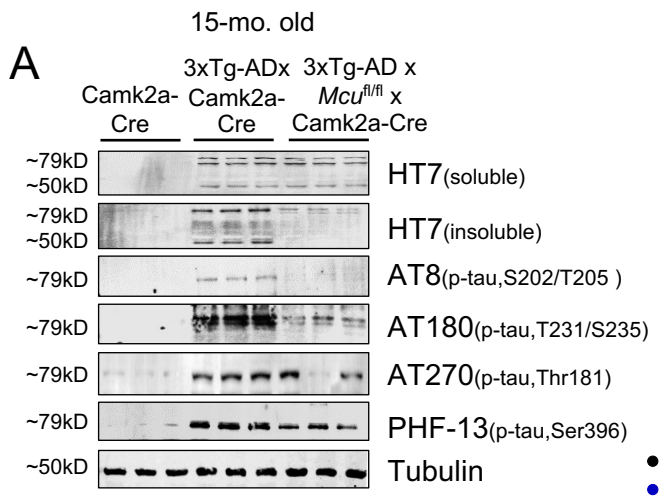
A
15-mo. old
Camk2a-Cre
3xTg-ADx Camk2a-Cre
3xTg-AD x Mcu fl/fl x Camk2a-Cre
~79kD
~50kD
HT7(soluble)
HT7(insoluble)
AT8(p-tau,S202/T205)
AT180(p-tau,T231/S235)
AT270(p-tau,Thr181)
PHF-13(p-tau,Ser396)
Tubulin

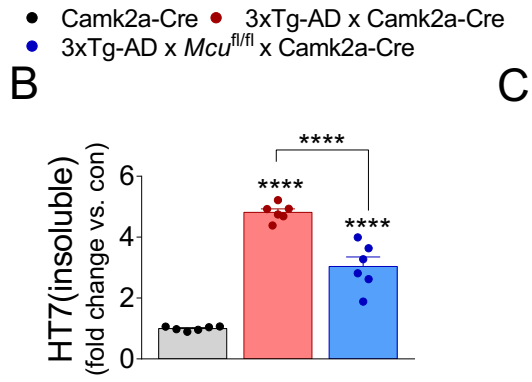
Camk2a-Cre
3xTg-AD x Camk2a-Cre
3xTg-AD x Mcu fl/fl x Camk2a-Cre
B
HT7(insoluble)
(fold change vs. con)
****
****
****

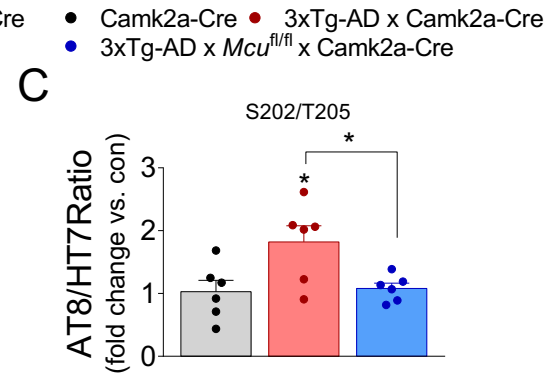
Camk2a-Cre
3xTg-AD x Camk2a-Cre
3xTg-AD x Mcu fl/fl x Camk2a-Cre
C
S202/T205
AT8/HT7Ratio
(fold change vs. con)
*
*

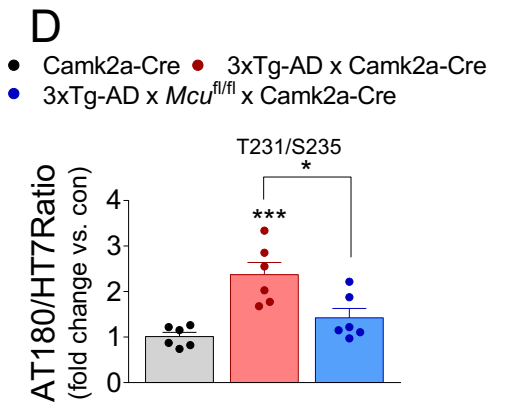
D
Camk2a-Cre
3xTg-AD x Camk2a-Cre
3xTg-AD x Mcu fl/fl x Camk2a-Cre
T231/S235
AT180/HT7Ratio
(fold change vs. con)
*
***

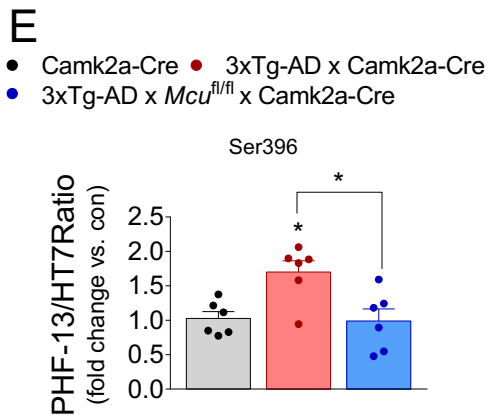
E
Camk2a-Cre
3xTg-AD x Camk2a-Cre
3xTg-AD x Mcu fl/fl x Camk2a-Cre
Ser396
PHF-13/HT7Ratio
(fold change vs. con)
*
*

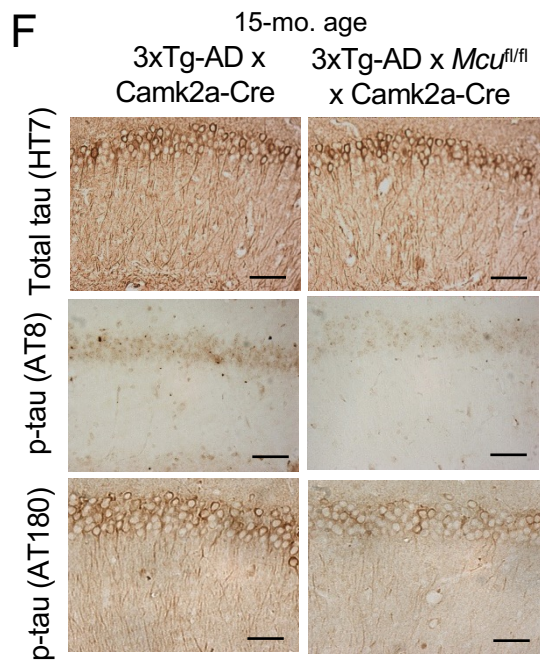
F
15-mo. age
3xTg-AD x Camk2a-Cre
3xTg-AD x Mcu fl/fl x Camk2a-Cre
Total tau (HT7)
p-tau (AT8)
p-tau (AT180)

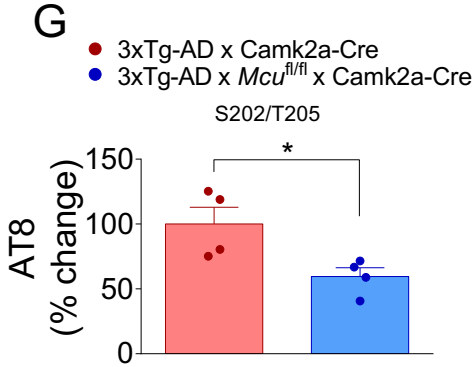
G
3xTg-AD x Camk2a-Cre
3xTg-AD x Mcu fl/fl x Camk2a-Cre
S202/T205
AT8
(% change)
*

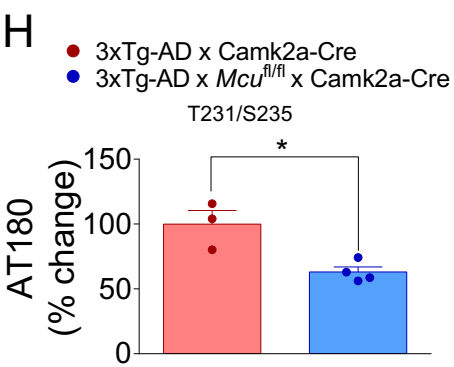
H
3xTg-AD x Camk2a-Cre
3xTg-AD x Mcu fl/fl x Camk2a-Cre
T231/S235
AT180
(% change)
*

Figure 4

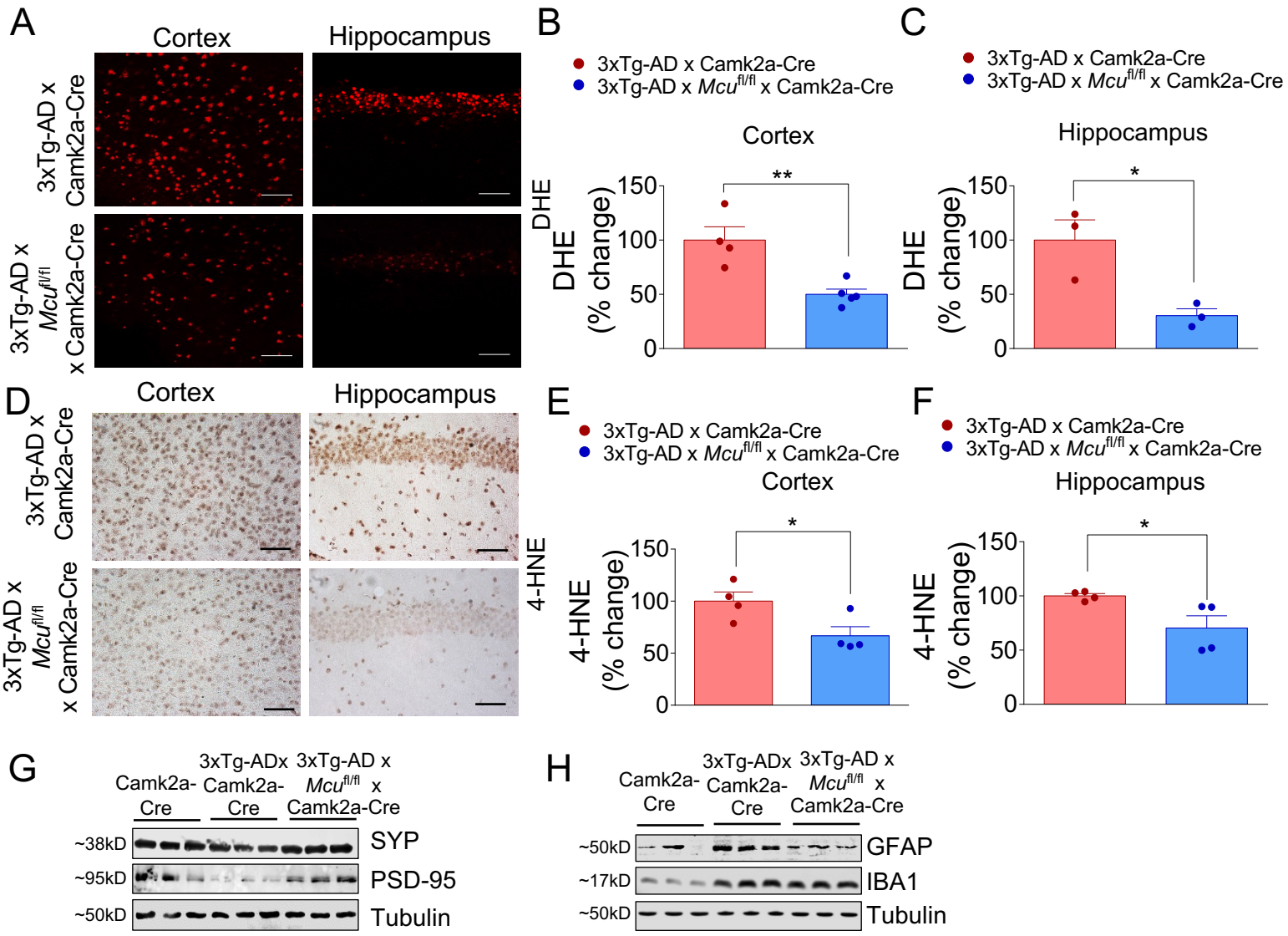
A
Cortex
Hippocampus
3xTg-AD x Camk2a-Cre
3xTg-AD x Mcu fl/fl x Camk2a-Cre
B
3xTg-AD x Camk2a-Cre
3xTg-AD x Mcu fl/fl x Camk2a-Cre
Cortex
DHE
DHE (% change)
150
100
50
0
**
C
3xTg-AD x Camk2a-Cre
3xTg-AD x Mcu fl/fl x Camk2a-Cre
Hippocampus
DHE
DHE (% change)
150
100
50
0
*
D
Cortex
Hippocampus
3xTg-AD x Camk2a-Cre
3xTg-AD x Mcu fl/fl x Camk2a-Cre
E
3xTg-AD x Camk2a-Cre
3xTg-AD x Mcu fl/fl x Camk2a-Cre
Cortex
4-HNE
4-HNE (% change)
150
100
50
0
*
F
3xTg-AD x Camk2a-Cre
3xTg-AD x Mcu fl/fl x Camk2a-Cre
Hippocampus
4-HNE
4-HNE (% change)
150
100
50
0
*
G
Camk2a-Cre
3xTg-ADx Camk2a-Cre
3xTg-AD x Mcu fl/fl x Camk2a-Cre
~38kD
SYP
~95kD
PSD-95
~50kD
Tubulin
H
Camk2a-Cre
3xTg-ADx Camk2a-Cre
3xTg-AD x Mcu fl/fl x Camk2a-Cre
~50kD
GFAP
~17kD
IBA1
~50kD
Tubulin

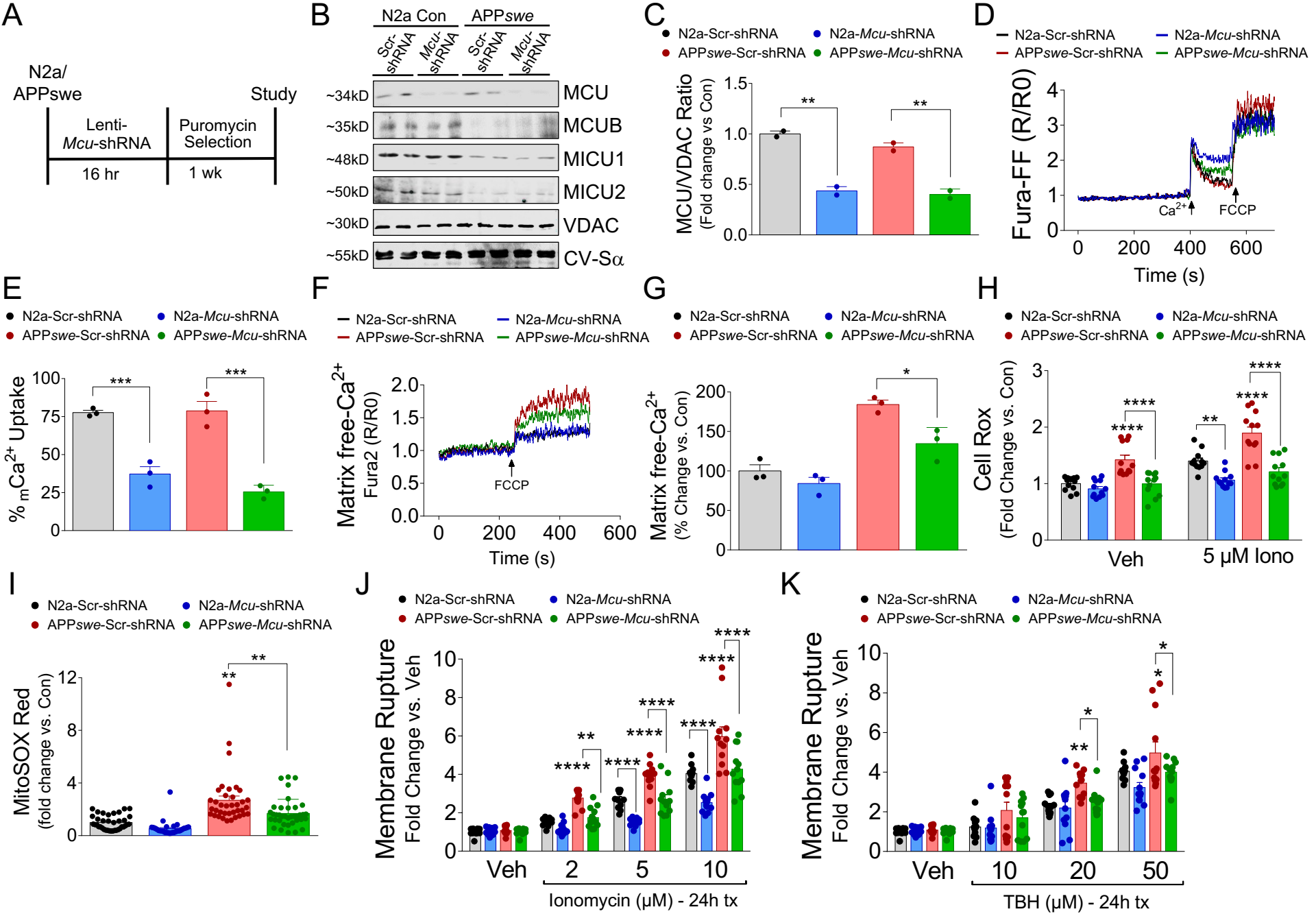
A
N2a/
APPswe
Study
Lenti-
Mcu-shRNA
Puromycin
Selection
16 hr
1 wk
B
N2a Con
APPswe
Scr-shRNA
Mcu-shRNA
Scr-shRNA
Mcu-shRNA
~34kD
MCU
~35kD
MCUB
~48kD
MICU1
~50kD
MICU2
~30kD
VDAC
~55kD
CV-Sα
C
N2a-Scr-shRNA
N2a-Mcu-shRNA
APPswe-Scr-shRNA
APPswe-Mcu-shRNA
MCU/VDAC Ratio
(Fold change vs Con)
D
Fura-FF (R/R0)
Ca2+
FCCP
Time (s)
E
% mCa2+ Uptake
F
Matrix free-Ca2+
Fura2 (R/R0)
FCCP
Time (s)
G
Matrix free-Ca2+
(% Change vs. Con)
H
Cell Rox
(Fold Change vs. Con)
Veh
5 μM Iono
I
MitoSOX Red
(fold change vs. Con)
J
Membrane Rupture
Fold Change vs. Veh
Veh
Ionomycin (μM) - 24h tx
K
Membrane Rupture
Fold Change vs. Veh
Veh
TBH (μM) - 24h tx

Figure 5